SUPPORTING INFORMATION

Photochemical Formation and Reversible Base-Induced Cleavage of a Phosphagallene

T. Taeufer,[a] F. Dankert,[a] D. Michalik,[a,b] J. Pospech,[a,*] J. Bresien,[b,*] C. Hering-Junghans[a,*]

(a) Dr. Tobias Taeufer, Dr. Fabian Dankert, Dr. Dirk Michalik, Dr. Jola Pospech, Dr. Christian Hering-Junghans

Leibniz Institut für Katalyse e.V. (LIKAT), A.-Einstein-Str. 29a, 18059 Rostock, Germany

(b) Dr. Dirk Michalik, Dr. Jonas Bresien

Institute of Chemistry, University of Rostock, A.-Einstein-Str. 3a, 18059 Rostock, Germany

This file includes:

1 Experimental

General Information. If not stated otherwise, all manipulations were performed under oxygen- and moisture-free conditions under an inert atmosphere of argon using standard Schlenk techniques or an inert atmosphere glovebox (MBraun LABstar ECO). All glassware was heated three times *in vacuo* using a heat gun and cooled under argon atmosphere. Solvents were transferred using syringes, steel- or PE-canulas, which were purged with argon prior to use. Solvents and reactants were either obtained from commercial sources or synthesized as detailed in Table S1.

Table S1: Origin and purification of solvents and reactants.

Substance	Origin	Purification
Benzene	local trade	dried over Na/benzophenone freshly distilled prior to use, stored over molecular sieves.
n-hexane	Geyer, CHROMASOLV®, for HPLC, ≥97,0% (GC)	purified with the Grubbs-type column system "Pure Solv MD-5" dried over Na/benzophenone/tetraglyme freshly distilled prior to use
n-pentane	local trade	dried over Na/benzophenone/tetraglyme freshly distilled prior to use
Toluene	Fisher Chemical, for HPLC	purified with the Grubbs-type column system "Pure Solv MD-5"
C_6D_6	euriso-top	dried over Na/benzophenone freshly distilled prior to use
C_7D_8 (toluene-d_8)	euriso-top	dried over Na/benzophenone freshly distilled prior to use
Cp*Ga[1]	synthesized	
^{Dip}TerPPMe$_3$[2]	synthesized	
^{Tip}TerPPMe$_3$[3]	synthesized	
PMe_3	Strem Chemicals, 98%	used as received

NMR spectra were recorded on Bruker spectrometers (AVANCE 300, AVANCE 400 or Fourier 300) and were referenced internally to the deuterated solvent (^{13}C: C_6D_6 δ_{ref} = 128.06 ppm; C_7D_8 δ_{ref} = 20.43 ppm) or to protic impurities in the deuterated solvent (^{1}H: C_6HD_5 δ_{ref} = 7.16 ppm; C_7D_8 δ_{ref} = 2.08 ppm). All measurements were carried out at ambient temperature unless denoted otherwise. NMR signals were assigned using experimental data (e.g. chemical shifts, coupling constants, integrals where applicable).

IR spectra of crystalline samples were recorded on a Bruker Alpha II FT-IR spectrometer equipped with an ATR unit at ambient temperature under argon atmosphere. Relative intensities are reported according to the following intervals: weak (w, 0–33%), medium (m, 33–66%), strong (s, 66–100%).

Elemental analyses were obtained using a Leco Tru Spec elemental analyzer.

UV-Vis spectra were acquired on an UV/Vis absorption spectrophotometer UV5 (Mettler Toledo) using Quartz glass cuvettes.

2 Structure elucidation

X-ray Structure Determination: X-ray quality crystals of **1a**, **1b** and **3** were selected in Fomblin© Y perfluoroether (Sigma Aldrich) at −30 °C under a constant stream of nitrogen. The samples were cooled to 150(2) K or 110(2) K (in case of **3**) during measurement. The data were collected on a Bruker Kappa Apex II diffractometer using Mo K_α radiation (λ = 0.71073 Å) or Cu K_α radiation (λ = 1.54178 Å). The structures were solved by iterative methods (SHELXT)[4] and refined by full matrix least squares procedures (SHELXL).[5] Semi-empirical absorption corrections were applied (SADABS).[6] All non-hydrogen atoms were refined anisotropically, hydrogen atoms were included in the refinement at calculated positions using a riding model.

Table S2: Crystallographic details of **1a**, **1b** and **3**.

Compound	**1a**	**1b**	**3**
Chem. Formula	$C_{40}H_{52}GaP$	$C_{46}H_{64}GaP$	$C_{31}H_{37}PO$
Formula weight [g/mol]	633.50	717.66	456.57
Colour	Blue	violet	Orange
Crystal system	monoclinic	triclinic	Monoclinic
Space group	$P2_1/c$	P-1	$P2_1/n$
a [Å]	10.1214(2)	10.6093(2)	11.9426(10)
b [Å]	22.1032(5)	12.7651(2)	18.1472(16)
c [Å]	16.8012(4)	20.7583(3)	12.6846(10)
α [°]	90	80.8620(10)	90
β [°]	106.0450(10)	81.8580(10)	98.094(3)
γ [°]	90	65.9260(10)	90
V [Å^3]	3612.27(14)	2524.95(7)	2721.7(4)
Z	4	2	4
$\rho_{calcd.}$ [g/cm^3]	1.165	0.944	1.114
μ [mm^{-1}]	1.628	1.208	1.028
T [K]	150(2)	150(2)	110(2)
Measured reflections	39411	32338	31222
Independent reflections	6280	8929	5099
Reflections with $I > 2\sigma(I)$	5377	8147	4831
R_{int}	0.0571	0.0283	0.0265
$F(000)$	1352	772	984
$R_1(R[F^2>2\sigma(F^2)])$	0.0344	0.0391	0.0342
w$R_2(F^2)$	0.0902	0.1109	0.0908
GooF	1.028	1.046	1.039
No. of Parameters	392	544	306
CCDC #	2216822	2216823	2216824

3 Syntheses of compounds

3.1 ^{Dip}TerPGaCp* (1a)

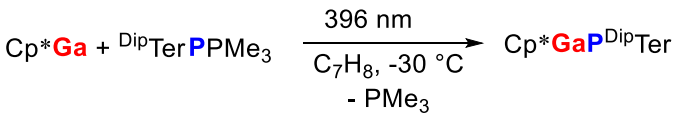

GaCp* (0.042 g, 0.21 mmol) and ^{Dip}TerPPMe$_3$ (0.102 g, 0.2 mmol) were dissolved in toluene (3 mL) in a 10 mL Schlenk tube and a magnetic stir bar was added. This Schlenk tube was connected via a U-glass tube with a second Schlenk tube and the reaction mixture was degassed (3x freeze/pump/thaw) and kept under static vacuum (10^{-3} mbar). The Schlenk tube with the reaction mixture was then placed in a cooling bath (iPrOH) cooled by a thermostat set at −30°C. The reaction mixture was then irradiated using two LED-panels (396 nm) for 4 h, resulting in a color change to dark green/blue. At this time the second Schlenk tube was placed in cooling bath (iPrOH: −70 °C) to slowly condense off the volatiles from the reaction mixture. This afforded after 24 h a dark green to blue solid on the glass walls of the reaction vessel. The solid was then washed with *n*-heptane (2 x 1 mL) at −78°C to give ^{Dip}TerP=GaCp* (**1a**, 0.098 g, 0.154 mmol, 77 %) as a dark greenish to blue solid. Storage of the *n*-heptane wash solution at −30 °C for 72 h afforded X-ray quality dark blue needles of **1a**.

CHN calc. (found) in %: C 75.83 (75.53), H 8.27 (8.28). **^{31}P{^{1}H} NMR** (C_6D_6, 162 MHz): δ = −105.5 ppm. **^{31}P{^{1}H} NMR** (122 MHz, C_7D_8, 298 K): δ = −104.8 ppm. **^{1}H NMR** (400 MHz, C_6D_6): δ = 1.13 (d, $^3J_{H,H}$ = 6.9 Hz, 12H, CH(C*H*$_3$)$_2$), 1.47 (d, $^3J_{H,H}$ = 6.9 Hz, 12H, CH(C*H*$_3$)$_2$), 1.50 (s, 15H, C$_5$(C*H*$_3$)$_5$), 3.02 (hept, $^3J_{H,H}$ = 6.7 Hz, C*H*(CH$_3$)$_2$), 6.86-6.93 (m, 3H, C*H*$_{Aryl}$), 7.19-7.23 (m, 4H, C*H*$_{Aryl}$), 7.25-7.29 (m, 2H, C*H*$_{Aryl}$). **^{1}H NMR** (300 MHz, C_7D_8, 298 K): δ = 1.11 (d, $^3J_{H,H}$ = 6.9 Hz, 12H, CH(C*H*$_3$)$_2$), 1.42 (d, $^3J_{H,H}$ = 6.9 Hz, 12H, CH(C*H*$_3$)$_2$), 1.51 (s, 15H, C$_5$(C*H*$_3$)$_5$), 2.94 (hept, $^3J_{H,H}$ = 6.9 Hz, 4H, C*H*(CH$_3$)$_2$), 6.76-6.92 (m, 3H, C*H*$_{Aryl}$),

7.14-7.21 (m, 4H, C*H*$_{Aryl}$), 7.21-7.28 (m, 2H, C*H*$_{Aryl}$). **^{13}C{^{1}H} NMR** (C_6D_6, 100.63 MHz): δ = 10.3 (d, $J_{P,C}$ = 3.6 Hz, $C_5(CH_3)_5$), 24.9 (d, $J_{P,C}$ = 2.1 Hz, $CH(CH_3)_2$), 25.2 ($CH(CH_3)_2$), 31.0 ($CH(CH_3)_2$), 117.7 ($C_5(CH_3)_5$), 119.9 (CH_{Aryl}), 124.5 (CH_{Aryl}), 127.7 (d, $J_{P,C}$ = 2.0 Hz, CH_{Aryl}), 128.8 (CH_{Aryl}), 140.6 (d, $J_{P,C}$ = 17.0 Hz, $C_{q,Aryl}$), 143.8 (d, $J_{P,C}$ = 3.4 Hz, $C_{q,Aryl}$), 147.9 ($C_{q,Aryl}$), 152.2 (d, $^{1}J_{P,C}$ = 83.7 Hz, $\underline{C}_qP$). **^{13}C{^{1}H} NMR** (C_7D_8, 75.5 MHz): δ = 10.1 (d, $J_{P,C}$ = 3.6 Hz, $C_5(CH_3)_5$), 24.8 (d, $J_{P,C}$ = 2.3 Hz, $CH(CH_3)_2$), 25.0 ($CH(CH_3)_2$), 30.9 ($CH(CH_3)_2$), 117.5 ($C_5(CH_3)_5$), 119.8 (CH_{Aryl}), 124.3 (CH_{Aryl}), 147.7 ($C_{q,Aryl}$). **IR** (ATR, neat, 32 scans, cm^{-1}): 3051 (w), 3019 (w), 2958 (m), 2922 (m), 2863 (m), 1572 (w), 1461 (m), 1444 (w), 1369 (m), 1359 (m), 1327 (w), 1309 (w), 1279 (w), 1247 (w), 1240 (w), 1175 (w), 1160 (w), 1146 (w), 1112 (w), 1079 (w), 1055 (w), 1036 (m), 1003 (w), 949 (w), 934 (w), 913 (w), 803 (m), 782 (m), 759 (s), 737 (m), 695 (w), 688 (w), 640 (w), 604 (w), 585 (w), 554 (w), 529 (w), 470 (s), 448 (m).

Figure S1: ^{1}H NMR spectrum of Cp*GaP^{Dip}Ter (**1a**) (400 MHz, C_6D_6, rt); 1.93 ppm: Cp*Ga.

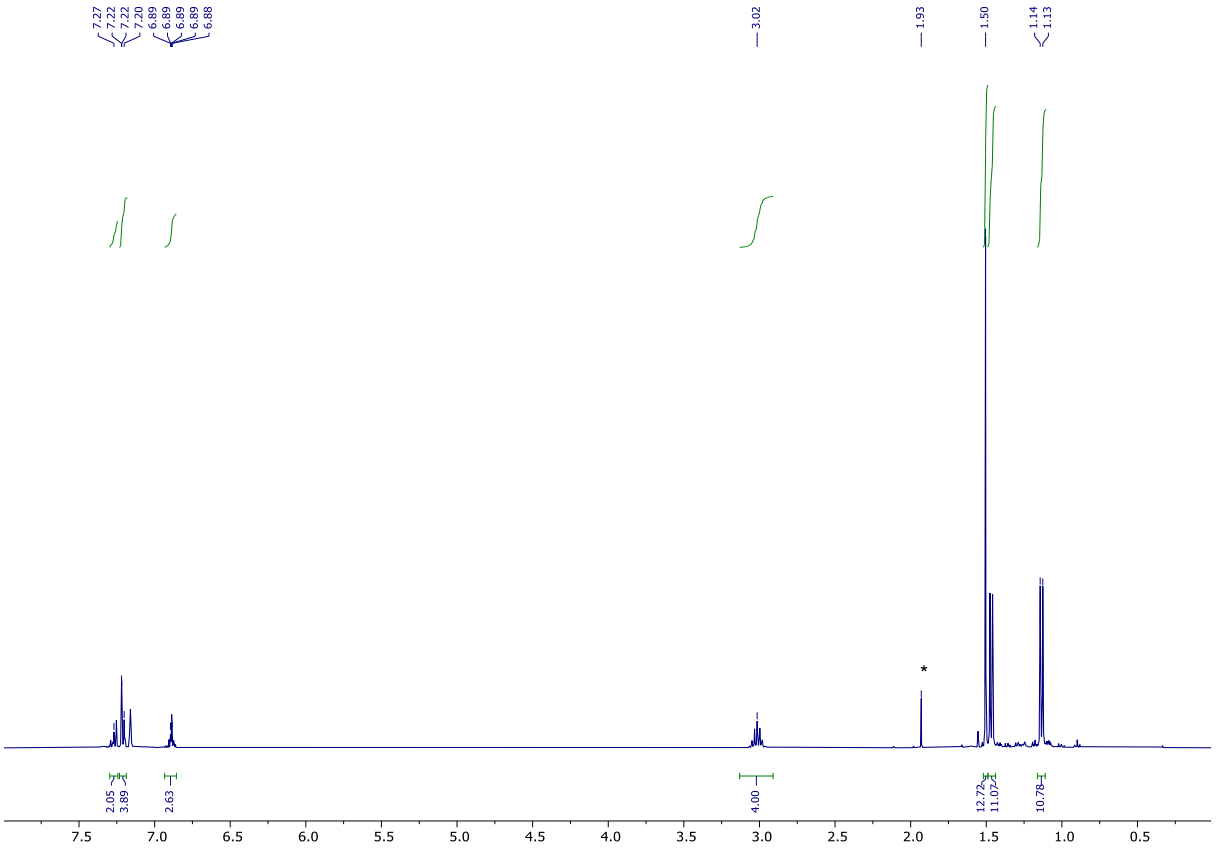

Figure S2: $^{13}C\{^{1}H\}$ NMR spectrum of Cp*GaP^{Dip}Ter (**1a**) (100.63 MHz, C_6D_6, rt).

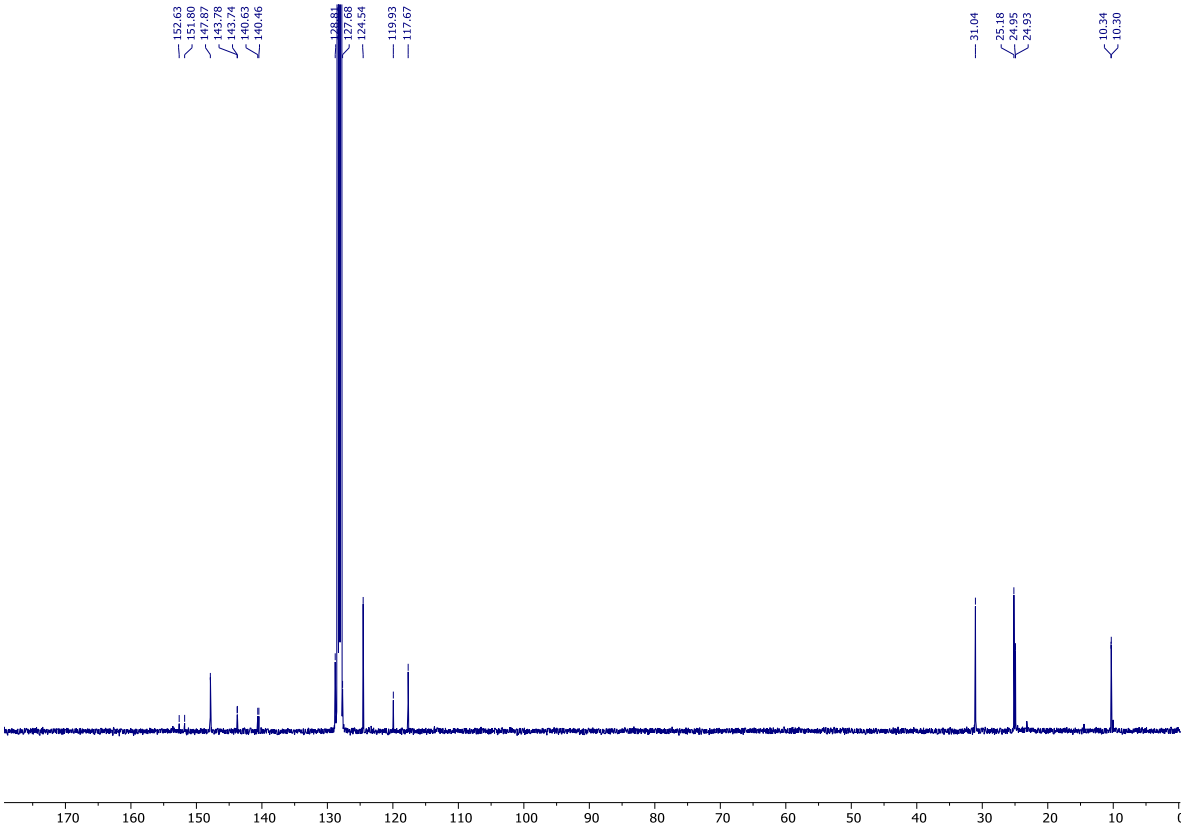

Figure S3: $^{31}P\{^{1}H\}$ NMR spectrum of Cp*GaP^{Dip}Ter (**1a**) (162.01 MHz, C_6D_6, rt).

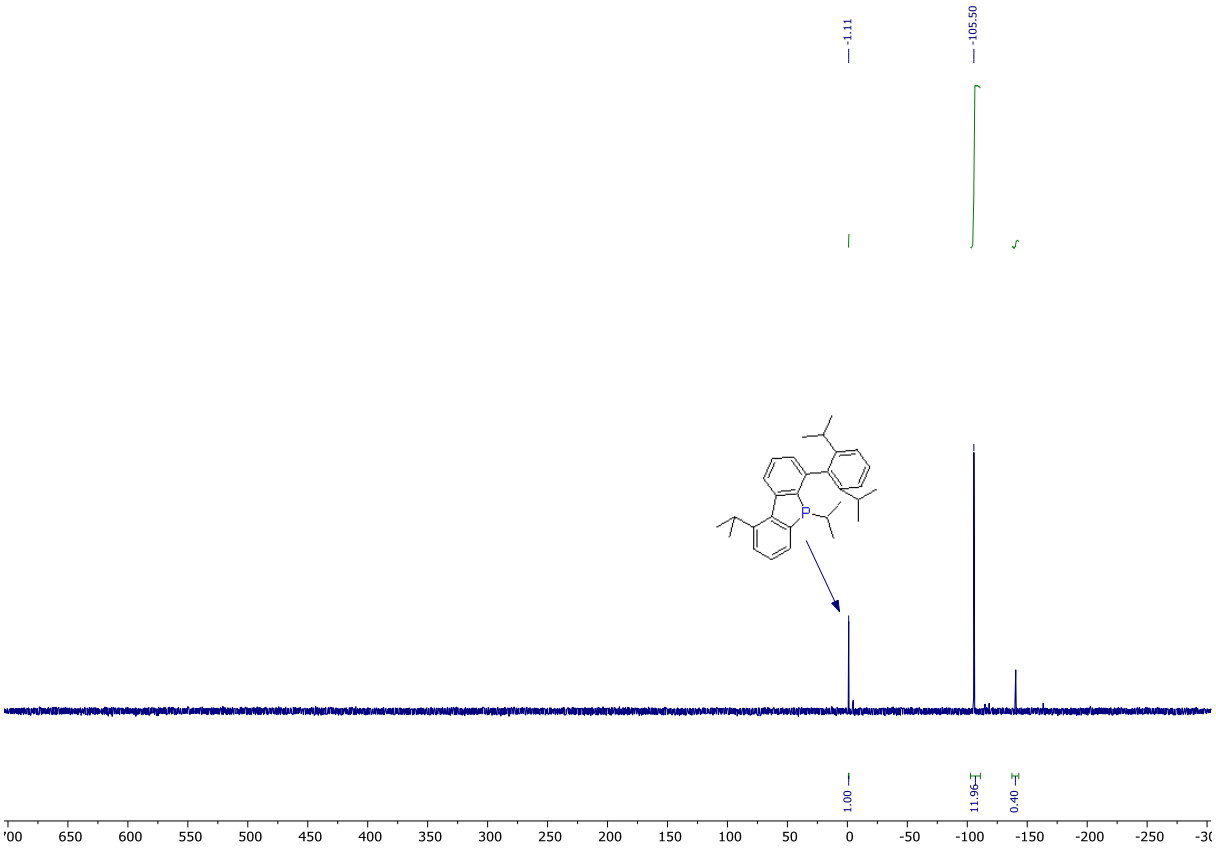

Figure S4: ^{1}H NMR spectrum of Cp*GaP^{Dip}Ter (**1a**) (400 MHz, C_7D_8, rt); 1.93 ppm: Cp*Ga.

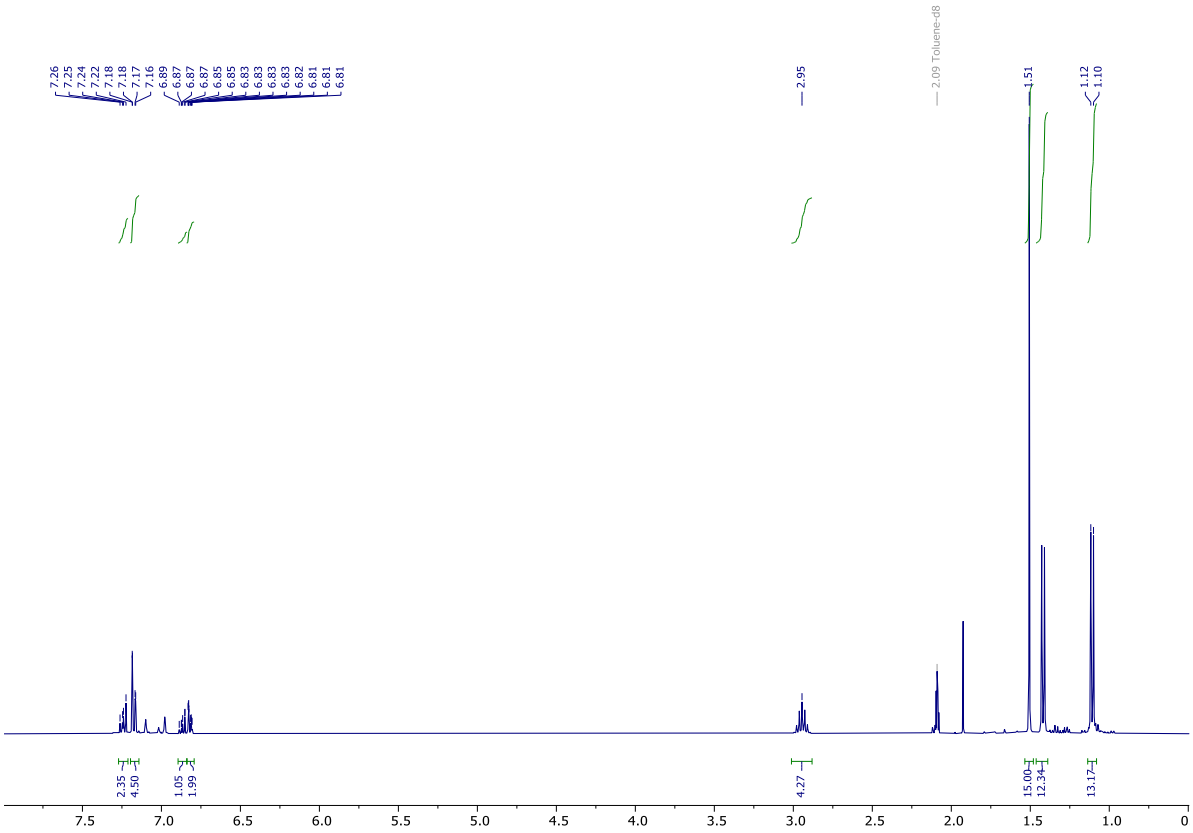

Figure S5: ^{13}C{^{1}H} NMR spectrum of Cp*GaP^{Dipp}Ter (**1a**) (75.49 MHz, C_7D_8, rt).

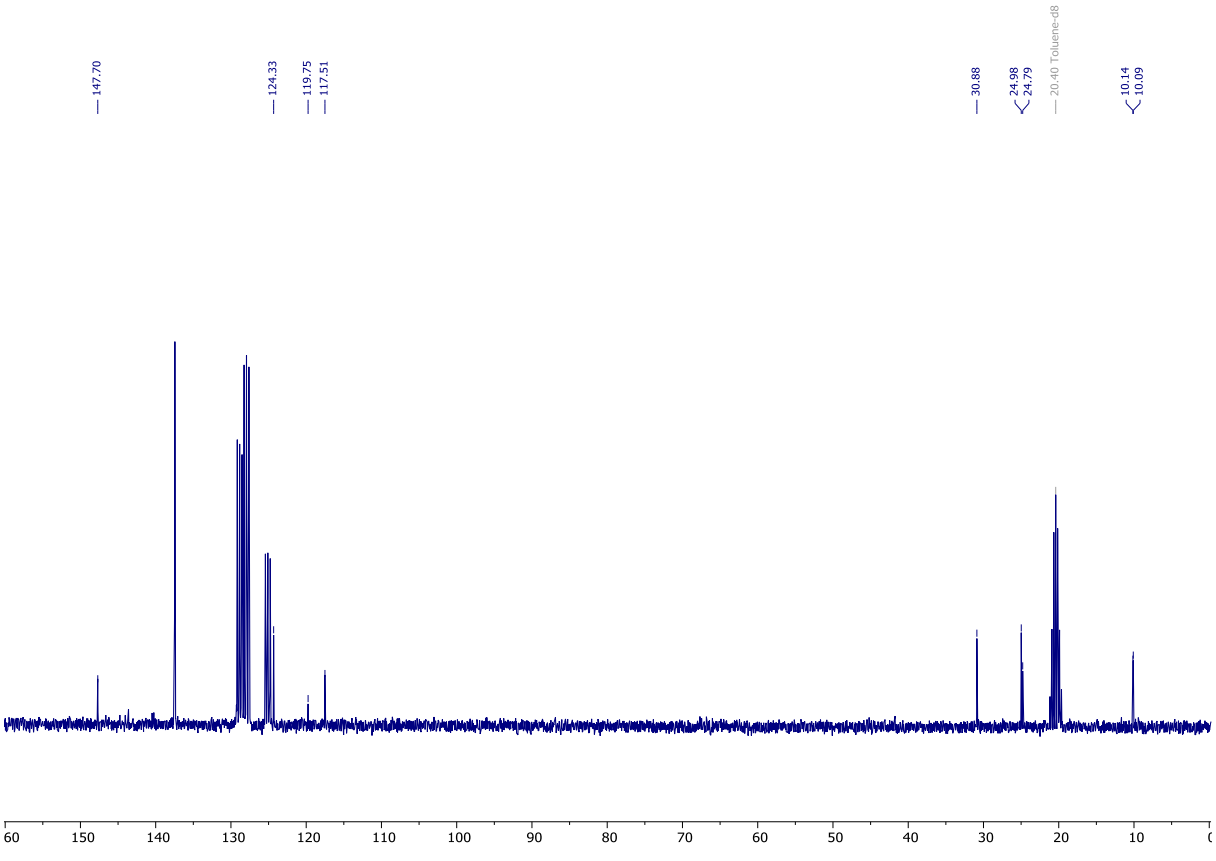

Figure S6: $^{31}P\{^{1}H\}$ NMR spectrum of Cp*GaP^{Dip}Ter (**1a**) (121.55 MHz, C_7D_8, rt).

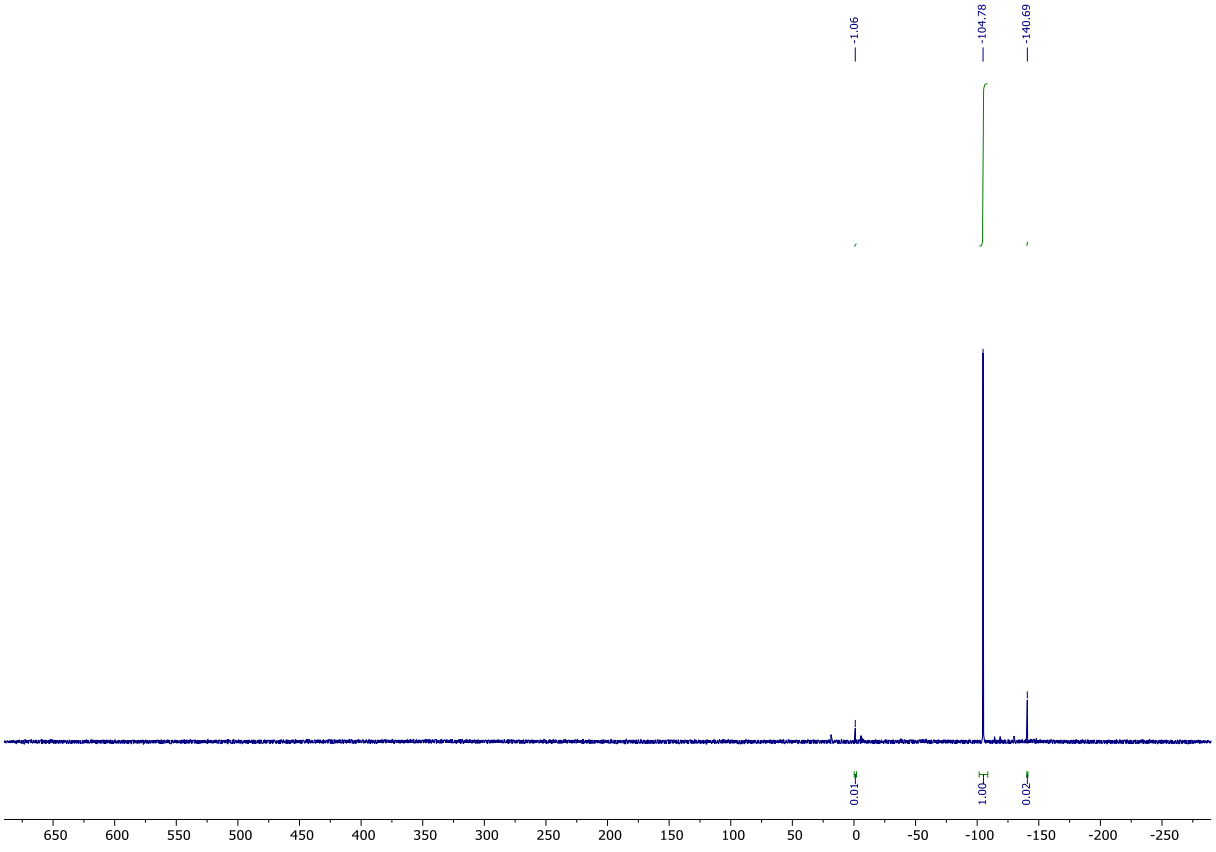

Figure S7: IR-spectrum of **1a** (ATR, neat, 32 scans, cm^{-1}).

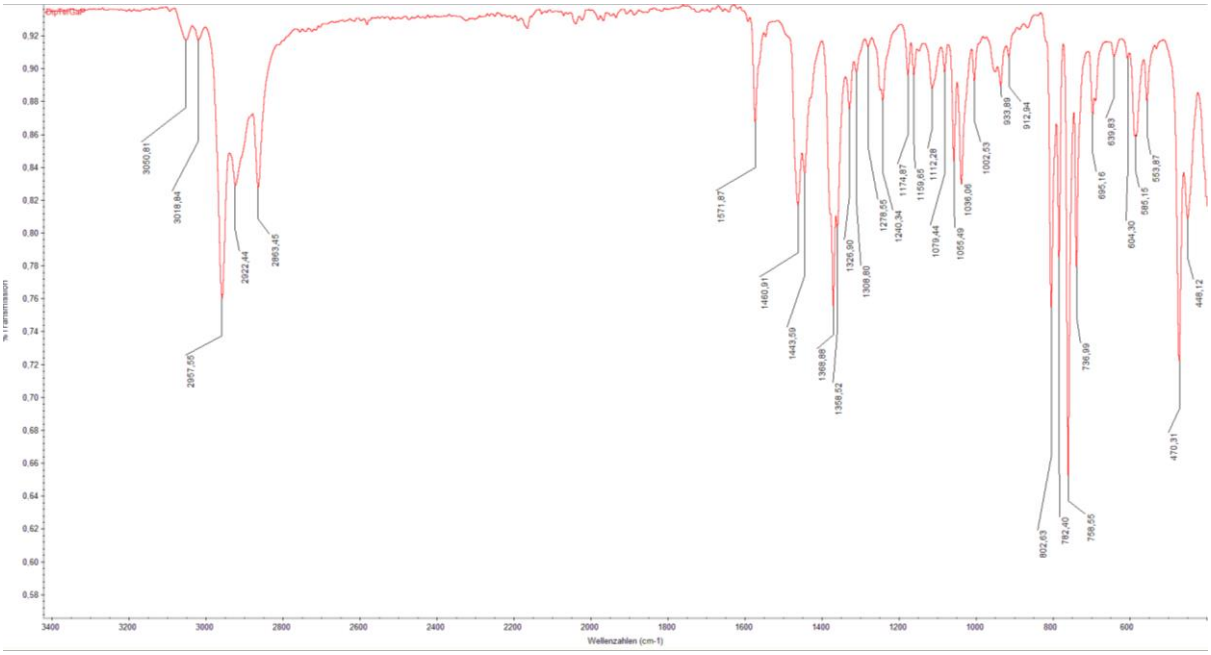

Figure S8: The decomposition of **1a** in toluene-d_8 solution follows first-order kinetics. In toluene-d_8, it has a half-life of 2866 ± 15 min at room temperature.

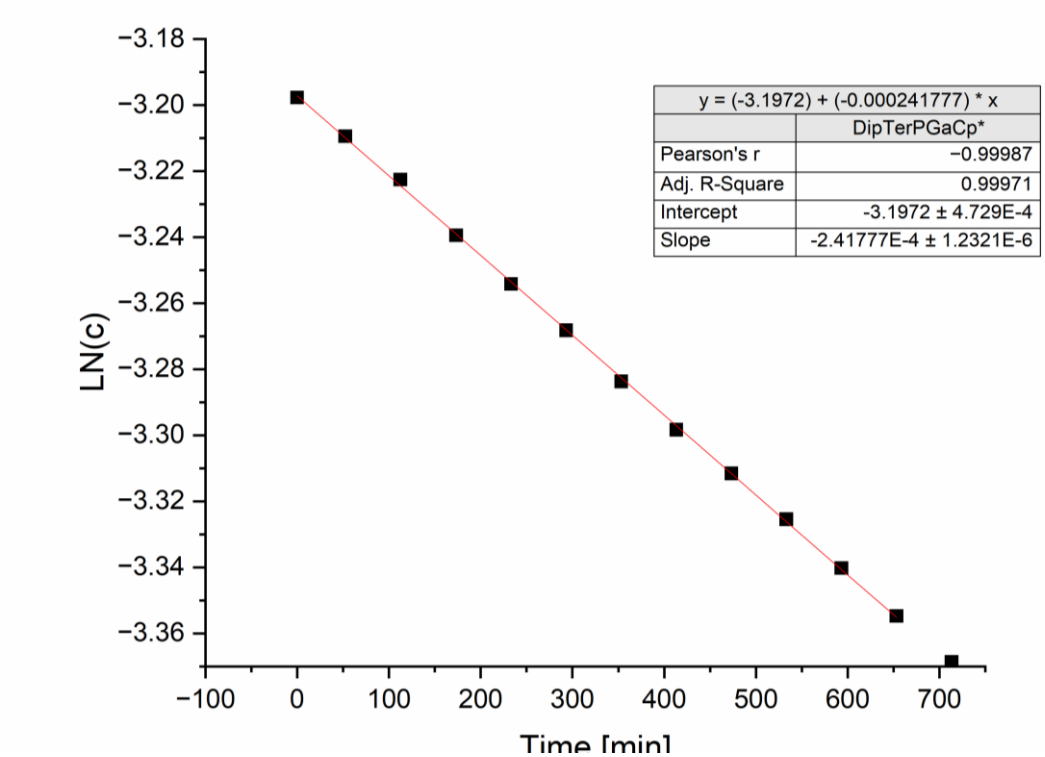

3.2 ^{Tip}TerPGaCp* (1b)

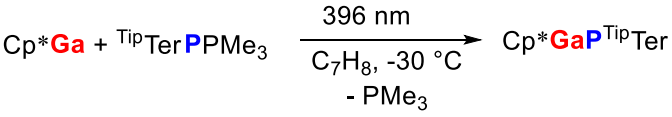

GaCp* (0.021 g, 0.10 mmol) and ^{Tip}TerPPMe$_3$ (0.059 g, 0.10 mmol) were dissolved in toluene (2 mL) in a 10 mL Schlenk tube and a magnetic stir bar was added. This Schlenk tube was connected via a U-glass tube with a second Schlenk tube and the reaction mixture was degassed (3x freeze/pump/thaw) and kept under static vacuum (10^{-3} mbar). The Schlenk tube with the reaction mixture was then placed in a cooling bath (iPrOH) cooled by a thermostat set at −30°C. The reaction mixture was then irradiated using two LED-panels (396 nm) for 4 h, resulting in a color change to dark green/blue. At this time the second Schlenk tube was placed in cooling bath (iPrOH:

−70 °C) to slowly condense off the volatiles from the reaction mixture. This afforded after 24 h a dark green to blue solid on the glass walls of the reaction vessel. The solid was then washed with minimal amounts of *n*-heptane (2 x 0.5 mL) to give ^{Tip}TerPGaCp* (**1b**, 0.035 g, 0.049 mmol, 49 %) as a dark green to blue solid. X-Ray quality crystals of **1b** were afforded when storing a saturated *n*-hexane solution of **1b** at −30 °C for 72 h.

CHN calc. (found) in %: C 76.98 (76.83), H 8.99 (9.13). **^{31}P{^{1}H} NMR** (C_6D_6, 122 MHz): δ = −109.8 ppm. **^{1}H NMR** (400 MHz, C_6D_6): δ = 1.20 (d, $^{3}J_{H,H}$ = 6.9 Hz, 12H, CH(C*H*)$_3$)$_2$), 1.28 (d, $^{3}J_{H,H}$ = 6.9 Hz, 12H, CH(C*H*)$_3$)$_2$), 1.53 (s, 15H, C_5(C*H*$_3$)$_5$), 1.54 (d, $^{3}J_{H,H}$ = 6.7 Hz, 12H, CH(C*H*)$_3$)$_2$), 2.88 (hept, $^{3}J_{H,H}$ = 6.9 Hz, C*H*(CH$_3$)$_2$), 3.09 (hept, $^{3}J_{H,H}$ = 6.9 Hz, C*H*(CH$_3$)$_2$), 6.84-6.77 (m, 3H, C*H*$_{Aryl}$), 7.26 (s, 4H, C*H*$_{Aryl}$). **^{13}C{^{1}H} NMR** (C_6D_6, 100.63 MHz): δ = 10.32 (d, $J_{P,C}$ = 3.6 Hz, C_5(*C*H$_3$)$_5$), 24.9 (d, $J_{P,C}$ = 2.1 Hz, CH(*C*H$_3$)$_2$), 25.2 (CH(*C*H$_3$)$_2$), 31.0 (*C*H(CH$_3$)$_2$), 117.7 (C_5(CH$_3$)$_5$), 122.6 (CH$_{Aryl}$), 128.6 (d, $J_{P,C}$ = 2.5 Hz, CH$_{Aryl}$), 129.3 (CH$_{Aryl}$), 140.6 (d, $J_{P,C}$ = 16.9 Hz, C$_{q,Aryl}$), 141.6 (d, $J_{P,C}$ = 3.1 Hz, C$_{q,Aryl}$), 147.8 (C$_{q,Aryl}$), 148.0 (C$_{q,Aryl}$),152.3 (d, $^{1}J_{P,C}$ = 80.5 Hz, C$_q$P). **IR** (ATR, neat, 32 scans, cm^{-1}): 3040 (w), 3025 (w), 2956 (s), 2923 (m), 2863 (m), 1603 (w), 1567 (w), 1458 (m), 1368 (s), 1359 (s), 1313 (w), 1247 (w), 1167 (w), 1152 (w), 1127 (w), 1099 (w), 1068 (w), 1051 (w), 1036 (w), 1002 (w), 938 (w), 921 (w), 876 (m), 849 (w), 788 (m), 772 (w), 757 (w), 732 (m), 719 (m), 650 (w), 586 (w), 540 (w), 514 (m), 453 (m).

Figure S9: ^{1}H NMR spectrum of Cp*GaP^{Tip}Ter (**1b**) (400 MHz, C_6D_6, rt); 2.11 ppm: toluene, 1.93 ppm: Cp*Ga, 0.90: *n*-hexane.

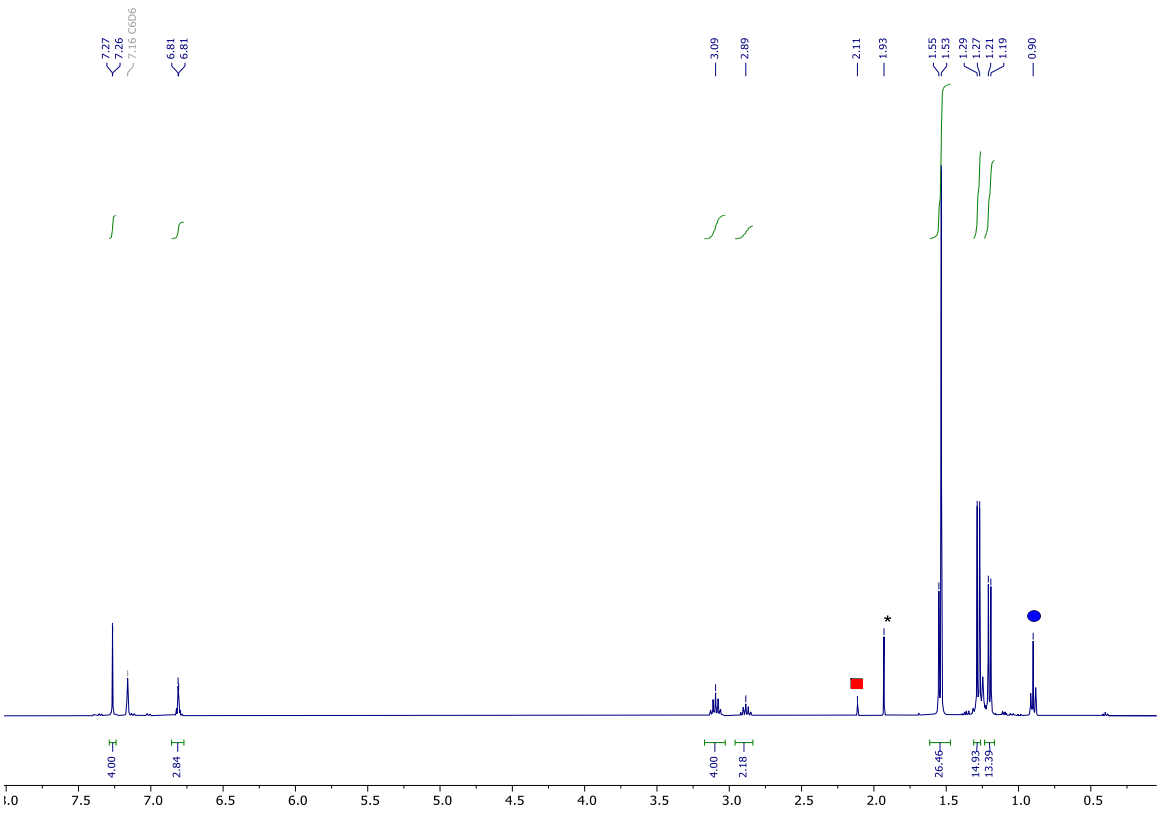

Figure S10: ^{13}C{^{1}H} NMR spectrum of Cp*GaP^{Tip}Ter (**1b**) (100.63 MHz, C_6D_6, rt).

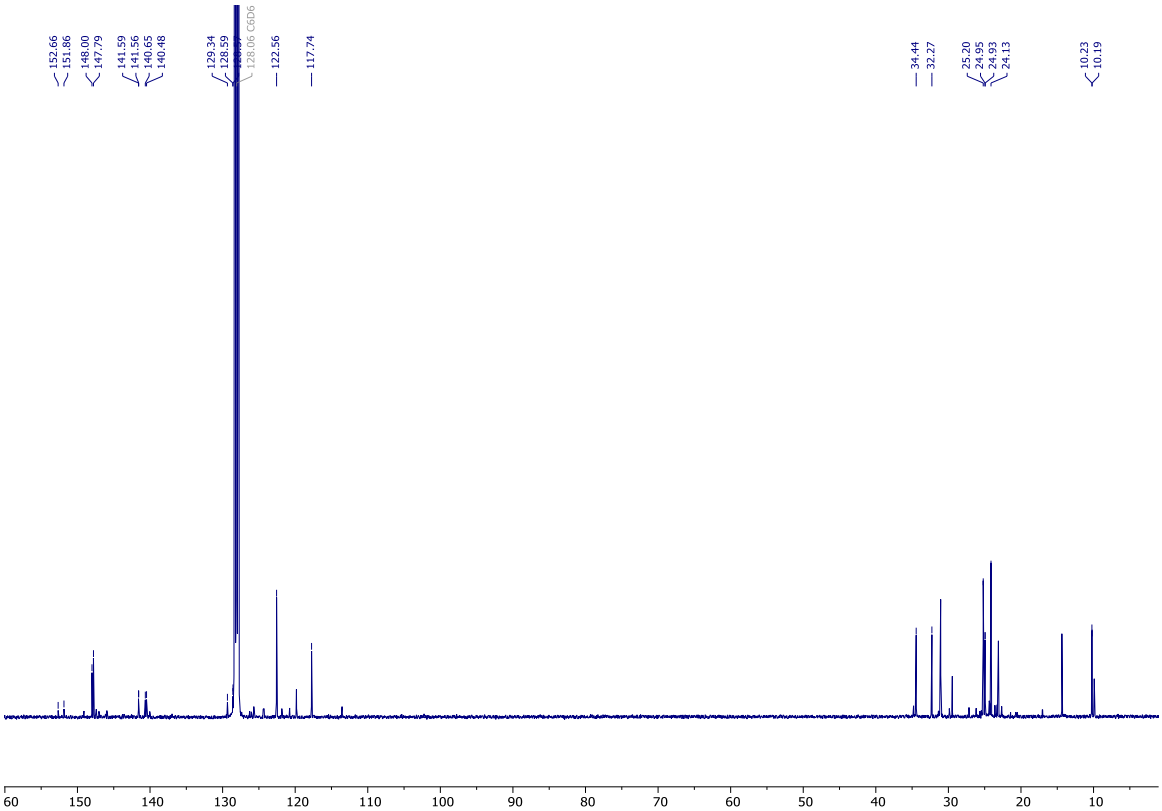

Figure S11: $^{31}P\{^{1}H\}$ NMR spectrum of ^{Tip}TerPGaCp* (**1b**) (162.01 MHz, C_6D_6, rt).

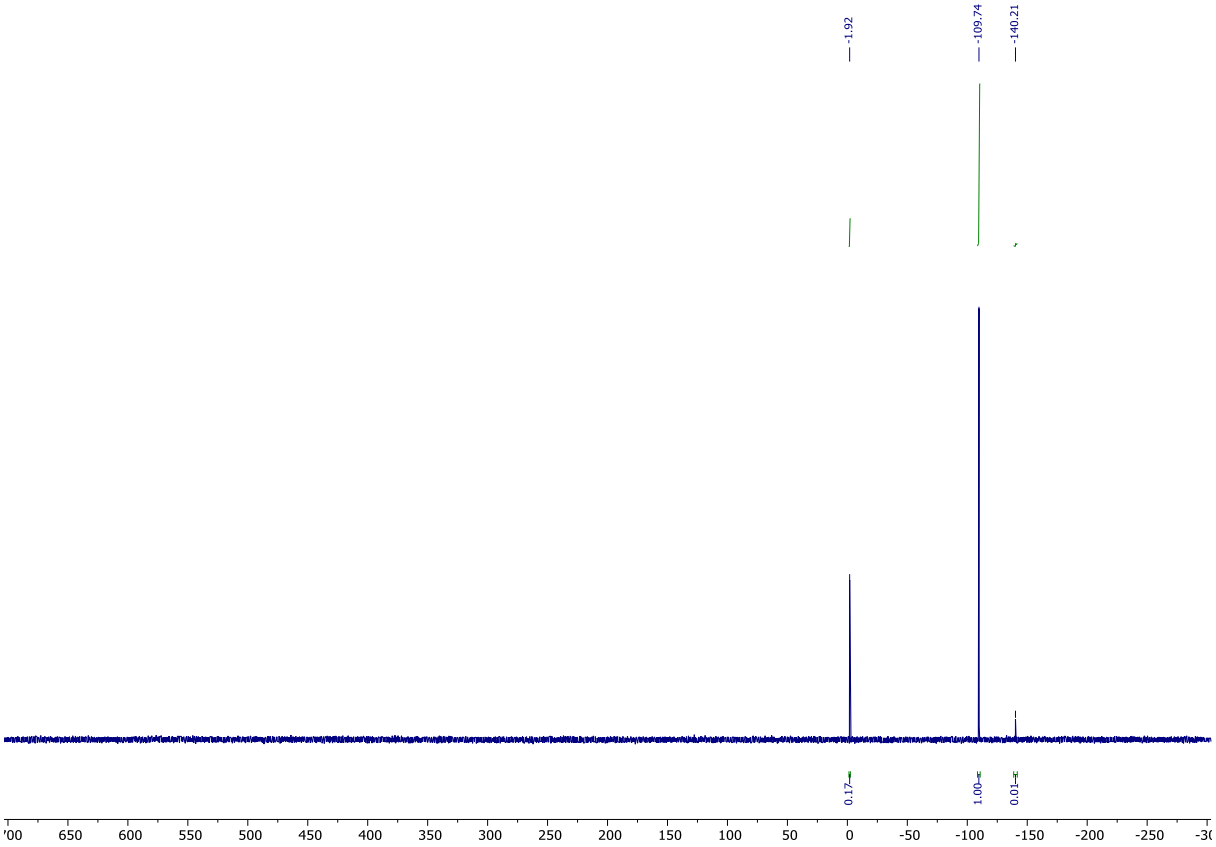

Figure S12: IR-spectrum of **1b** (ATR, r.t., 32 scans).

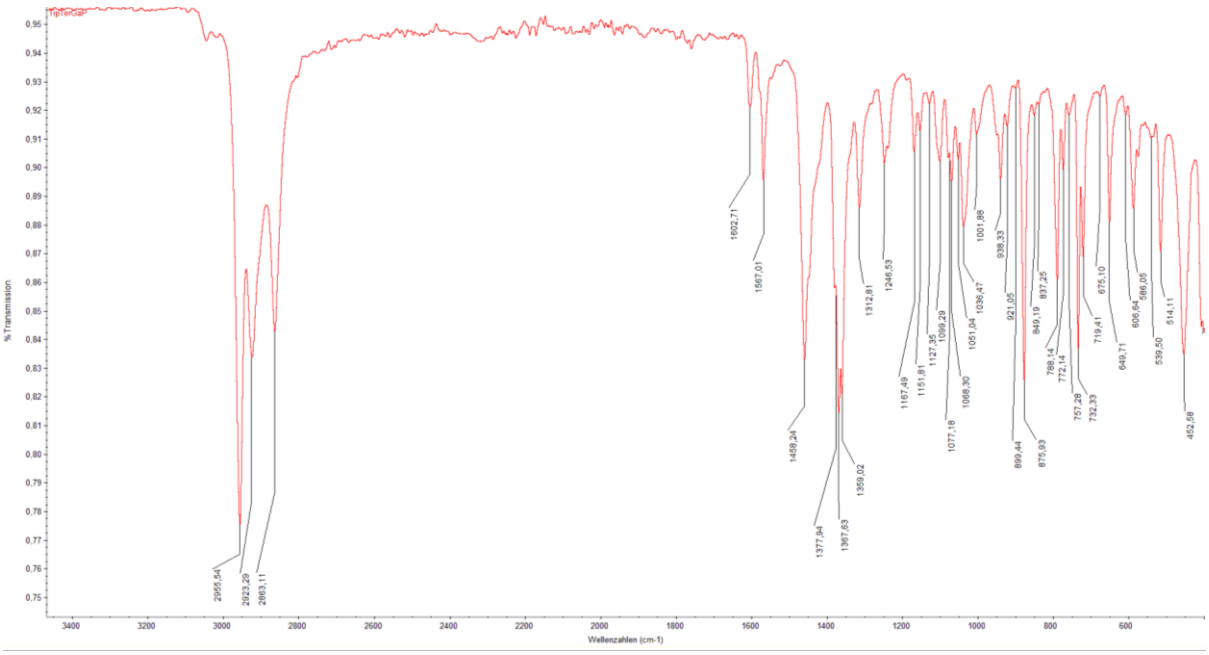

Figure S13: The decomposition of **1b** in toluene-d_8 solution follows first-order kinetics. In toluene-d_8, it has a half-life of 475 ± 11 min at room temperature.

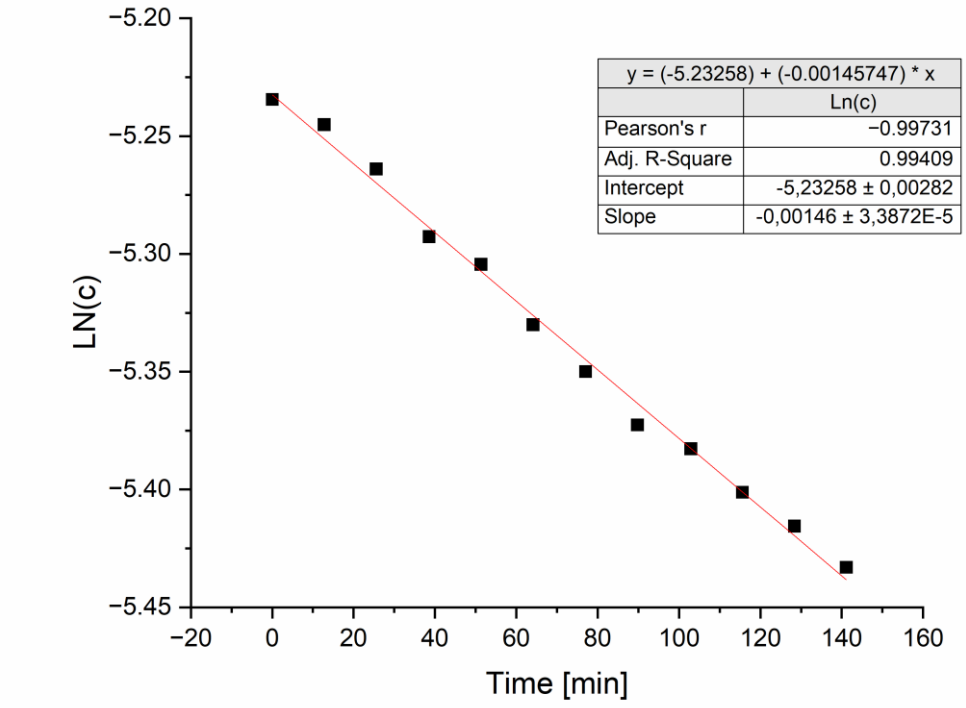

3.3 Thermal decomposition of ^{Dip}TerPGaCp* (1a)

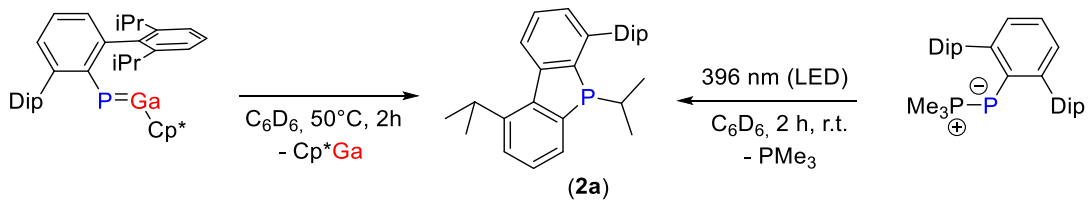

1a (0.020 g, 0,032 mmol) was dissolved in toluene-d_8 (0.5 mL), giving a deeply coloured green/blue solution, and was transferred into an NMR tube fitted with a J-Young valve. The NMR tube was placed in an oil bath (50 °C) for 2 h, which resulted in decolorization, giving an opaque clear solution, which according to $^{31}P\{1H\}$ NMR spectroscopy afforded the phosphafluorene **2a**.

2a can also be accessed via irradiation of ^{Dip}TerP(PMe$_3$) (0.025 g, 0.05 mmol) in toluene-d$_8$ solution using two LED-panels (396 nm) for 2 h at r.t. This afforded **2a** in quantitative fashion according to ^{31}P{^{1}H} NMR spectroscopy.

2a was only characterized by multinuclear NMR spectroscopy.

^{31}P{^{1}H} NMR (C_7D_8, 162 MHz): δ = −1.1 ppm. **^{1}H NMR** (400 MHz, C_7D_8): δ = 8.16 (dd, J = 8.1, 0.8 Hz, 1H, C*H*$_{Aryl}$), 7.44-7.36 (m, 2H, C*H*$_{Aryl}$), 7.33-7.28 (m, 2H, C*H*$_{Aryl}$), 7.26-7.22 (m, 1H, C*H*$_{Aryl}$), 7.20-7.11 (m, 3H, C*H*$_{Aryl}$), 3.92 (hept, $^3J_{HH}$ = 6.8 Hz, 1H, C*H*(CH$_3$)$_2$), 2.92 (hept, $^3J_{HH}$ = 6.8 Hz, 1H, C*H*(CH$_3$)$_2$), 2.66 (hept, $^3J_{HH}$ = 6.8 Hz, 1H, C*H*(CH$_3$)$_2$), 1.97 – 1.83 (m, 1H, C*H*(CH$_3$)$_2$), 1.37 (d, $^3J_{HH}$ = 6.8 Hz, 3H, CH(C*H*$_3$)$_2$), 1.30 (d, $^3J_{HH}$ = 6.7 Hz, 3H, CH(C*H*$_3$)$_2$), 1.26 (d, $^3J_{HH}$ = 6.8 Hz, 3H, CH(C*H*$_3$)$_2$), 1.16 (d, $^3J_{HH}$ = 6.7 Hz, 3H, CH(C*H*$_3$)$_2$), 1.12 (d, $^3J_{HH}$ = 6.8 Hz, 3H, CH(C*H*$_3$)$_2$), 1.08-1.00 (m, 3H, CH(C*H*$_3$)$_2$), 0.98 (d, $^3J_{HH}$ = 6.8 Hz, 3H, CH(C*H*$_3$)$_2$), 0.29 (t, $^3J_{HH}$ = 6.6 Hz, 3H, CH(C*H*$_3$)$_2$). **^{13}C{^{1}H} NMR** (C_7D_8, 100.6 MHz): δ = 147.13 (d, J_{PC} = 33.3 Hz), 146.00, 145.98, 143.38 (d, J_{PC} = 4.0 Hz), 143.31, 142.12 (d, J_{PC} = 6.3 Hz), 141.86, 138.84 (d, J_{PC} = 2.3 Hz), 128.53 – 128.32 (m), 126.85 (d, J_{PC} = 8.5 Hz), 125.62, 124.80, 123.78, 122.70, 31.2 (d, J_{PC} = 4.5 Hz), 30.8, 29.8, 27.0, 26.0, 25.5, 25.3, 23.4, 23.2, 22.9 (d, J_{PC} = 5.7 Hz), 22.4, 16.9 (d, J_{PC} = 5.7 Hz).

Figure S14: ^{1}H NMR spectrum of phosphafluorene **2a** (400 MHz, C_7D_8, rt); 0.79 PMe_3.

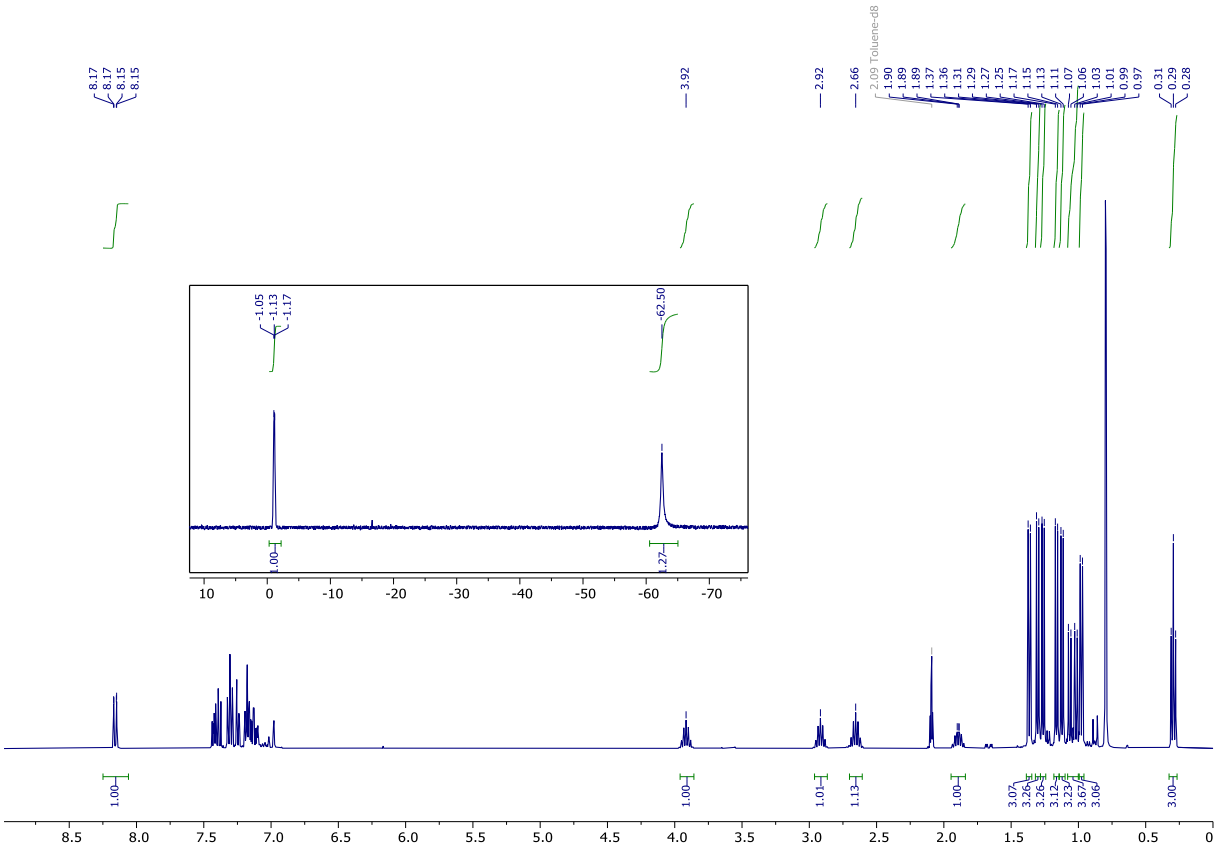

Figure S15: $^{13}C\{^{1}H\}$ NMR spectrum of phosphafluorene **2a** (100.63 MHz, C_7D_8, rt).

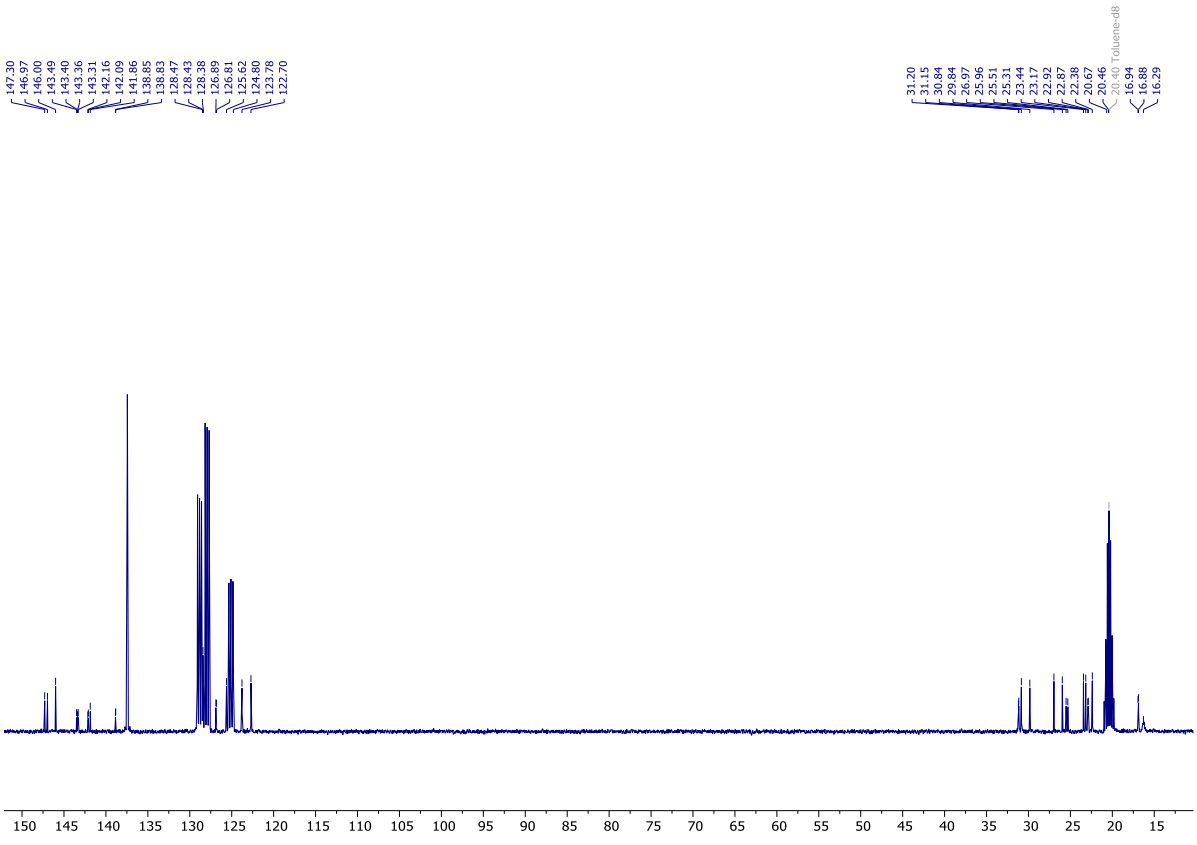

Figure S16: $^{31}P\{^{1}H\}$ NMR spectrum of phosphafluorene **2a** (162.01 MHz, C_7D_8, rt; −62.5 ppm: PMe_3).

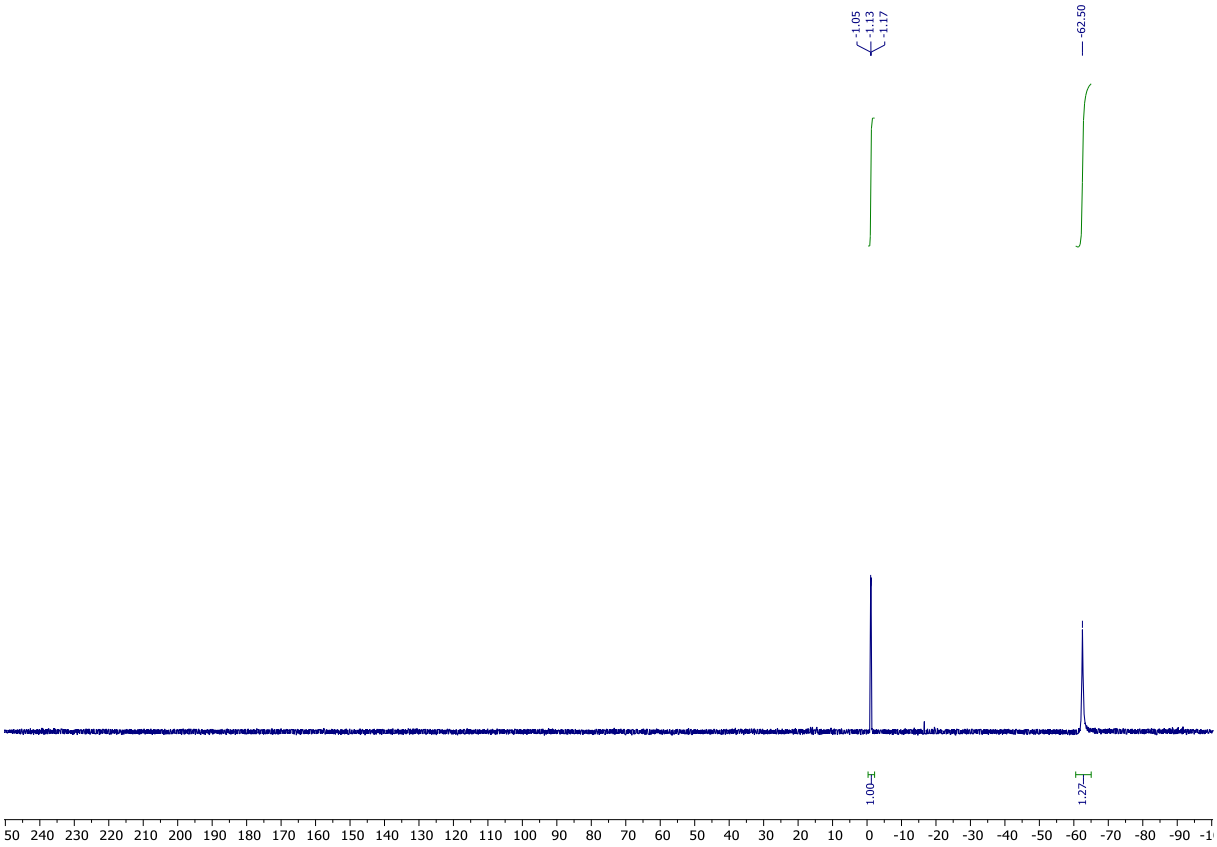

3.4 Reactivity of ^{Dip}TerPGaCp* towards CO_2: ^{Dip}TerPCO (3)

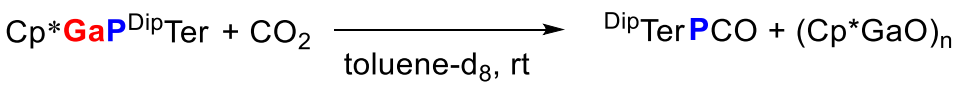

A 10 mL Schlenk tube (10 mL) was charged with a portion of **1a** (0.030 g, 0.049 mmol) and toluene-d_8 (0.7 mL) was added, affording a deep greenish to blue solution. On a Schlenk line this solution was exposed to CO_2 gas over a period of 20 min at room temperature resulting in a colour change from green to bright orange. The reaction solution was then transferred into an NMR tube equipped with a J-Young screw cap.

The NMR tube was then brought into a Glovebox and was transferred into a vial and the solvents were removed in vacuo. The orange solid froth was taken on in *n*-hexane (0.3 mL) and the cloudy solution was filtered through a pipette equipped with a microfiber glass filter paper, giving a clear orange solution. Storage at −30 °C for a

period of 7 d afforded minimal amounts of orange plates of ^{Dip}TerPCO (**3**) suitable for SC-XRD experiments. It was not possible to isolate enough material for a comprehensive analytical characterization. However, multinuclear NMR spectroscopy clearly underlines that **3** is formed selectively and in quantitative fashion, beside various Cp*GaO-containing species (δ(^{1}H) = 1.65-2.02 ppm).

^{31}P{^{1}H} NMR (122 MHz, C_7D_8, 298 K): δ = −201.3 ppm. **^{1}H NMR** (300 MHz, C_7D_8, 298 K): δ = 1.06 (d, $^3J_{H,H}$ = 6.8 Hz, 12H, CH(CH_3)$_2$), 1.33 (d, $^3J_{H,H}$ = 6.9 Hz, 12H, CH(CH_3)$_2$), 2.75 (hept, $^3J_{H,H}$ = 6.9 Hz, 4H, CH(CH$_3$)$_2$), 6.93-7.06 (m, 3H, CH_{Aryl})*, 7.07-7.20 (m, 4H, *m*-CH_{Dip}), 7.31 (dd, J_{HH} = 8.3, 7.2 Hz, 2H, *p*-CH_{Dip}). *overlap with toluene-d$_8$ signals. **^{13}C{^{1}H} NMR** (C_7D_8, 100.63 MHz): δ = 199.86 (d, $^1J_{PC}$ = 102.4 Hz, Ar-P<u>C</u>O), 147.64 (*o*-C$_{Dip}$), 146.59 (d, $^1J_{PC}$ = 45.0 Hz, *ipso*-C$_{Ar}$), 144.85 (d, $^2J_{PC}$ = 17.8 Hz, *o*-C$_{Ar}$), 140.31 (d, $^3J_{PC}$ = 5.4 Hz, *ipso*-C$_{Dip}$), 133.18 (d, $^3J_{PC}$ = 35.9 Hz, *m*-<u>C</u>$_{Ar}$H), 130.29, 126.55, 123.61 (C$_{Ar}$H), 31.09 (<u>C</u>H(CH$_3$)$_2$), 24.99 (CH(<u>C</u>H$_3$)$_2$), 23.79 (d, J_{PC} = 1.5 Hz, CH(<u>C</u>H$_3$)$_2$).

Figure S17: ^{1}H NMR spectrum of phosphaketene **3** (300 MHz, C_7D_8, rt).

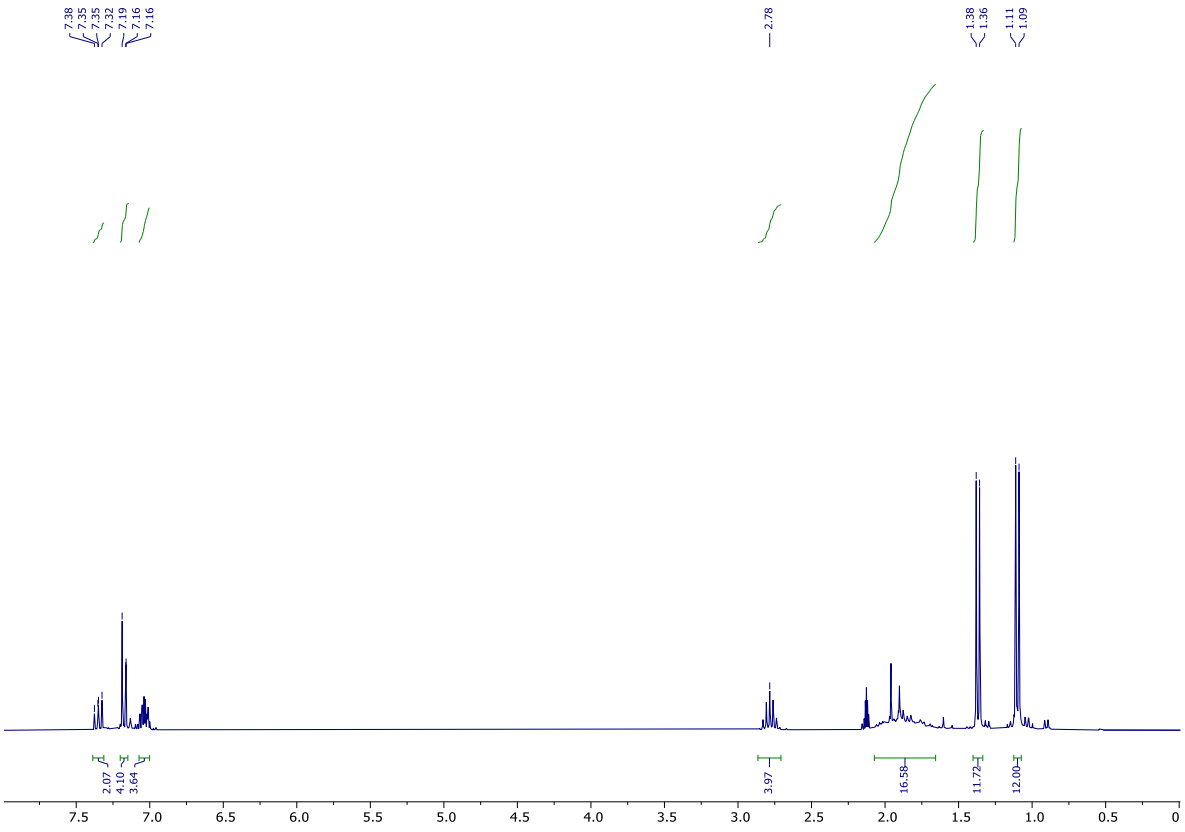

Figure S18: $^{13}C\{^{1}H\}$ NMR spectrum of phosphaketene **3** (100.63 MHz, C_7D_8, rt).

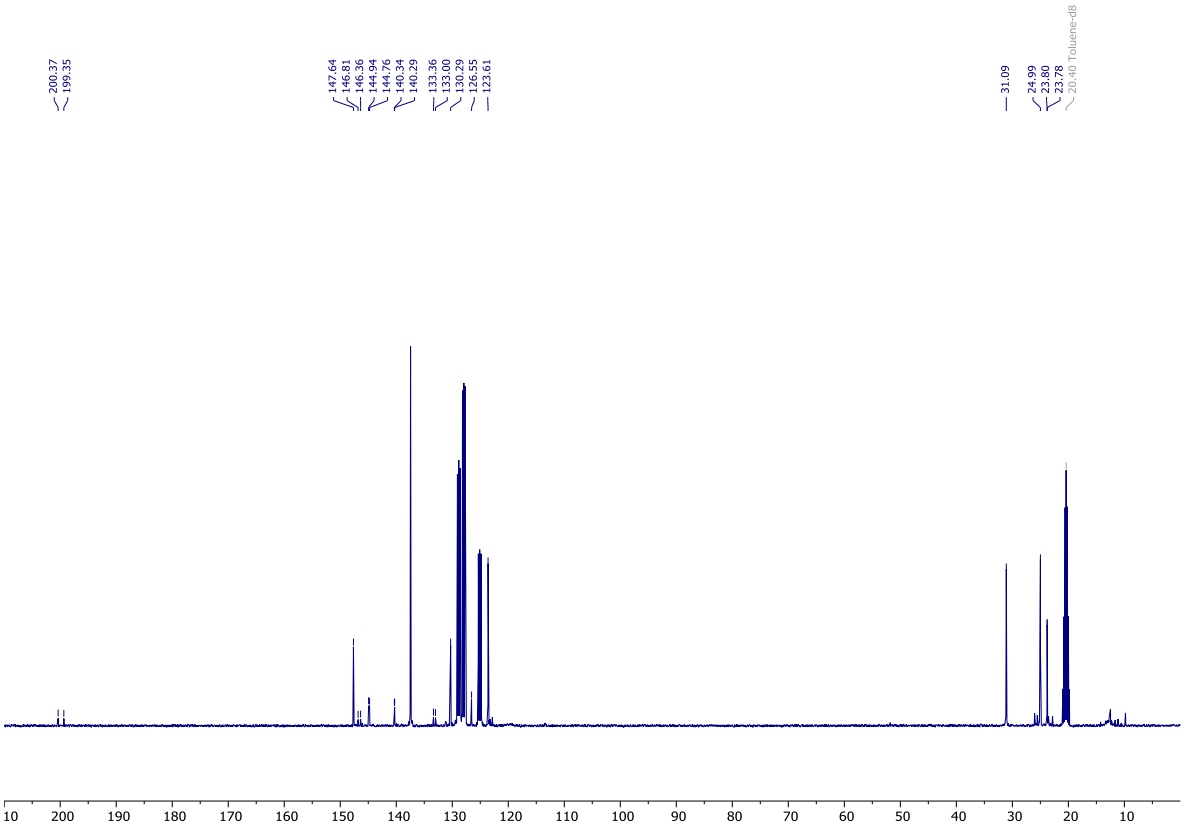

Figure S19: $^{31}P\{^{1}H\}$ NMR spectrum of phosphaketene **3** (121.55 MHz, C_7D_8, rt).

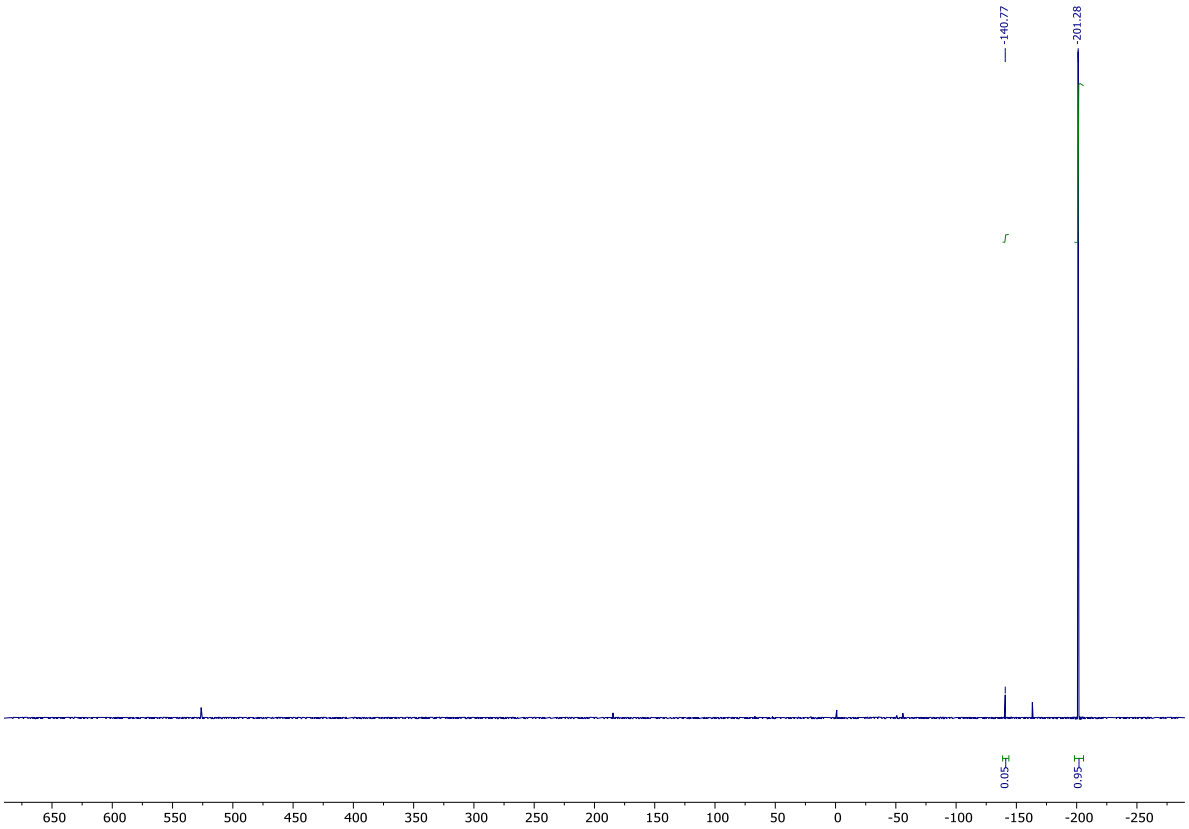

3.5 Reactivity of ^{Dip}TerPGaCp* towards H_2O: ^{Dip}TerPH$_2$ (4)

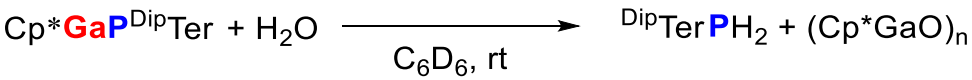

To a solution of **1a** in C_6D_6 (0.5 mL) a drop of degassed water was added, affording a clear pale-yellow solution. NMR spectroscopy showed full conversion into ^{Dip}TerPH$_2$ and several Cp*GaO-containing species. The NMR data of ^{Dip}TerPH$_2$ matches the literature values.[7]

^{31}P{^{1}H} NMR (122 MHz, C_6D_6, 298 K): δ = −140.5 ppm. **^{1}H NMR** (300 MHz, C_6D_6, 298 K): δ = 1.10 (d, $^3J_{H,H}$ = 6.8 Hz, 12H, CH(C*H*$_3$)$_2$), 1.29 (d, $^3J_{H,H}$ = 6.9 Hz, 12H, CH(C*H*$_3$)$_2$), 2.78 (hept, $^3J_{H,H}$ = 6.9 Hz, 4H, C*H*(CH$_3$)$_2$), 3.28 (d, $^1J_{P,H}$ = 211.0 Hz, Ar-P*H*$_2$), 7.02-7.13 (m, 3H, C*H*$_{Aryl}$), 7.07-7.20 (m, 4H, *m*-C*H*$_{Dip}$), 7.31 (dd, J_{HH} = 8.3, 7.2 Hz, 2H, *p*-C*H*$_{Dip}$).

Figure S20: ^{1}H NMR spectrum of ^{Dip}TerPH$_2$ (**4**) (300 MHz, C_6D_6, rt, reaction mixture).

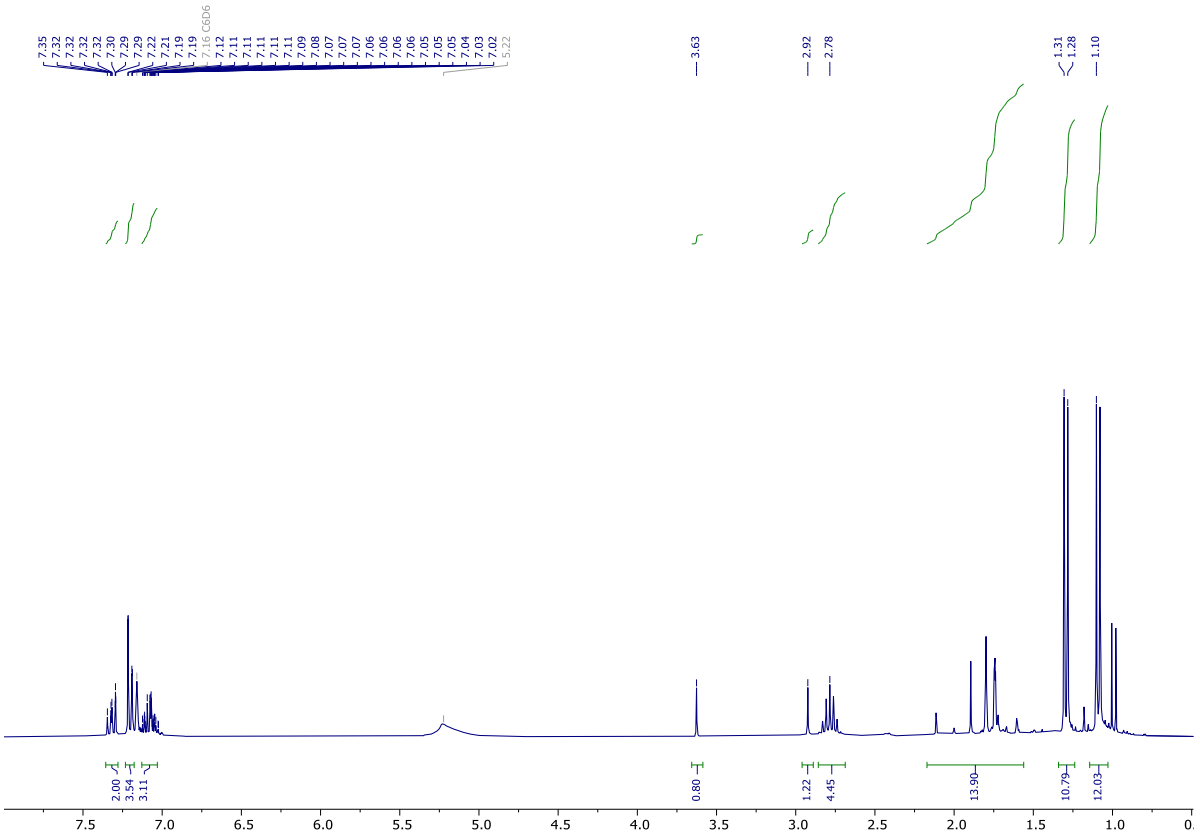

Figure S21: $^{31}P\{^{1}H\}$ NMR spectrum of $^{Dip}TerPH_2$ (**4**) (121.55 MHz, C_6D_6, rt).

4 Additional spectroscopic details

4.1 UV-vis spectra and extinction coefficients

UV-vis spectra of the starting materials Cp*Ga, ^{Dip}TerP(PMe$_3$) and ^{Tip}TerP(PMe$_3$) and the corresponding phosphagallenes **1a** and **1b** were recorded in *n*-hexane. The UV-vis cuvettes were filled in the Glovebox and sealed with NMR septa.

Saturation was reached even at very low concentrations below 360 nm for **1a** and **1b**. We therefore focused on a characteristic absorption in the visible region located at ca. 633 nm for both **1a** (full width half maximum FWHM is 200 nm) and **1b** (full width half maximum FWHM is 197 nm).

Figure S22: UV-vis spectra of **Cp*Ga** (c = 0.16 mg/mL, in *n*-hexane at room temperature (absorption maxima see Table S4).

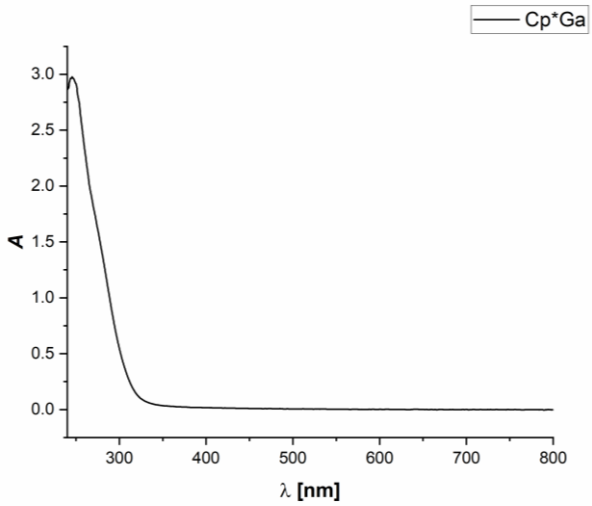

Table S3. Absorption maxima λ_{max} and experimental extinction coefficients ε for **Cp*Ga**.

Compnd.	**λ_{max} [nm]**	**ε [l·mol^{-1}·cm^{-1}]**
Cp*Ga	246	3805.92

Figure S23: UV-vis spectra of **DipTerP(Me$_3$)** (c = 0.24 mg/mL, left) and **^{Tip}TerP(PMe$_3$)** (c = 0.24 mg/mL, right) in *n*-hexane at room temperature (absorption maxima see Table S4).

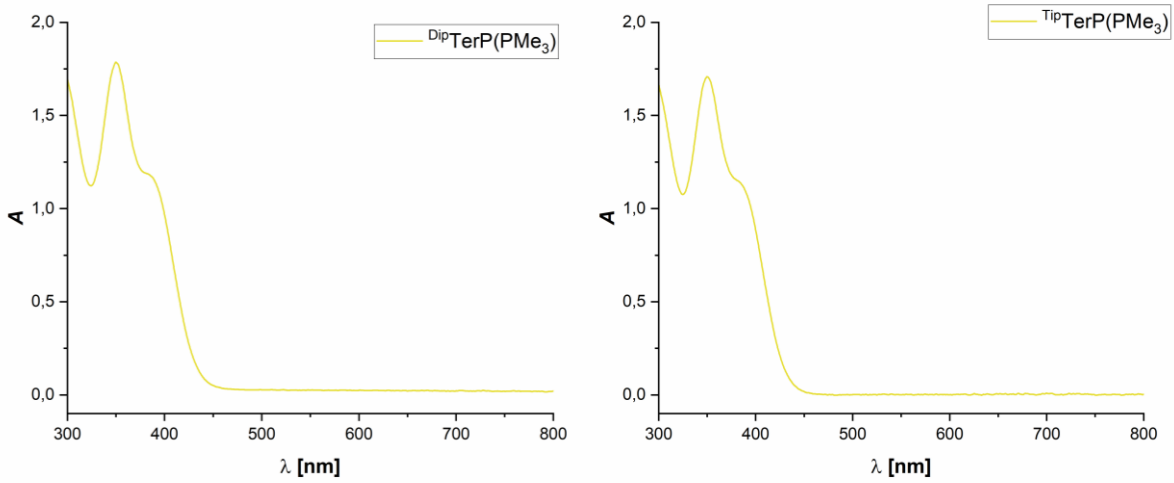

Table S4. Absorption maxima λ_{max} and experimental extinction coefficients ε for **^{Dip}TerP(PMe$_3$)** and **^{Tip}TerP(PMe$_3$)**.

Compnd.	λ_{max} [nm]	ε [l·mol^{-1}·cm^{-1}]
^{Dip}TerP(PMe$_3$)	350	4382.8
	381	2920.5
^{Tip}TerP(PMe$_3$)	350	4234.8
	381	2854.1

Figure S24: UV-vis spectra of **1a** (c = 0.17 mg/mL, left) and **1b** (c = 0.20 mg/mL, right) in *n*-hexane at room temperature (absorption maxima see Table S5).

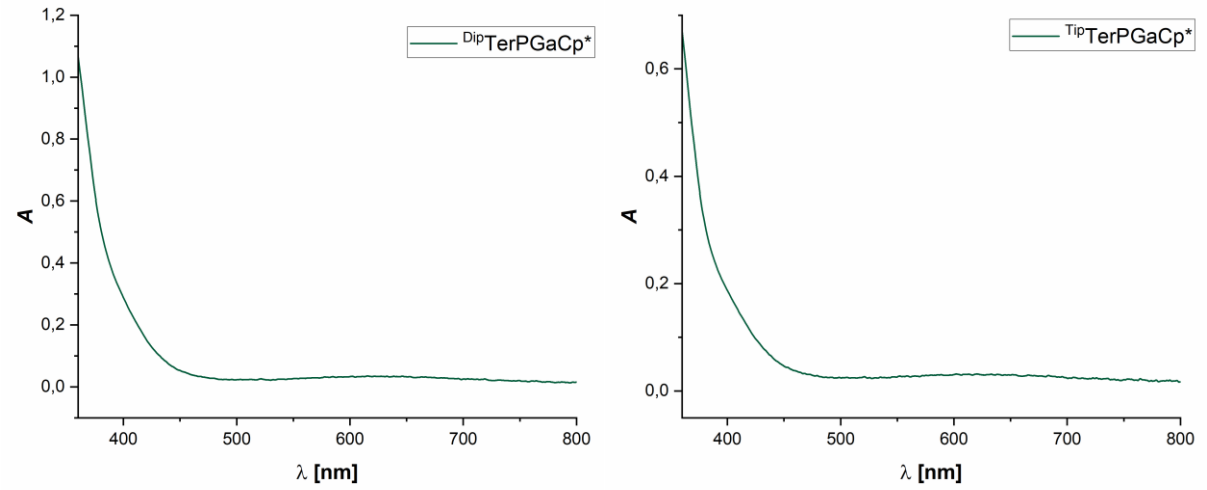

Table S5. Absorption maxima λ_{max} and experimental extinction coefficients ε for **^{Dip}TerPGaCp*** (**1a**) and **^{Tip}TerPGaCp*** (**1b**).

Compnd.	**λ_{max} [nm]**	**ε [l·mol^{-1}·cm^{-1}]**
1a	633	128.6
1b	633	112.3

4.2 Kinetic studies using NMR spectroscopy

To gain further insight into the photoreaction of **^{Dip}TerP(PMe$_3$)** with **Cp*Ga** as well as the thermal cleavage of **^{Dip}TerP=GaCp*** (**1a**) in the presence of **PMe$_3$**, a series of time-resolved ^{1}H and ^{31}P NMR spectra were recorded at different temperatures, under irradiation at 405 nm (−20, −10 °C; 140 mA diode current) as well as in the dark (10, 15, 20, 25 °C).

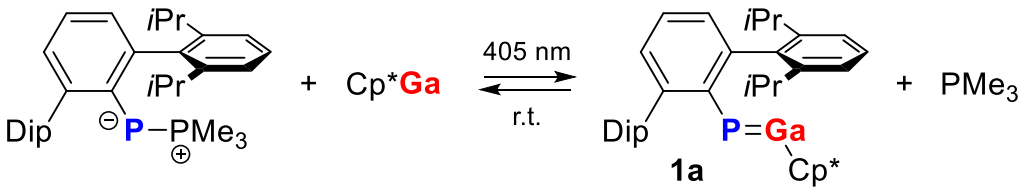

Figure S25 and Figure S26 show exemplary *in situ* ^{1}H and ^{31}P{^{1}H} NMR spectra of the photoreaction (measured under irradiation at 405 nm) as well as the thermal reverse reaction (measured in the dark). The ^{1}H integrals were used to quantify the concentrations of all involved species. Exemplary concentration profiles are plotted in Figure S27 –Figure S31.

Figure S25: In situ ^{1}H (left) and ^{31}P{^{1}H} (right) NMR spectra of the photoreaction of **^{Dip}TerP(PMe$_3$)** with **Cp*Ga** at −20 °C (irradiation at 405 nm).

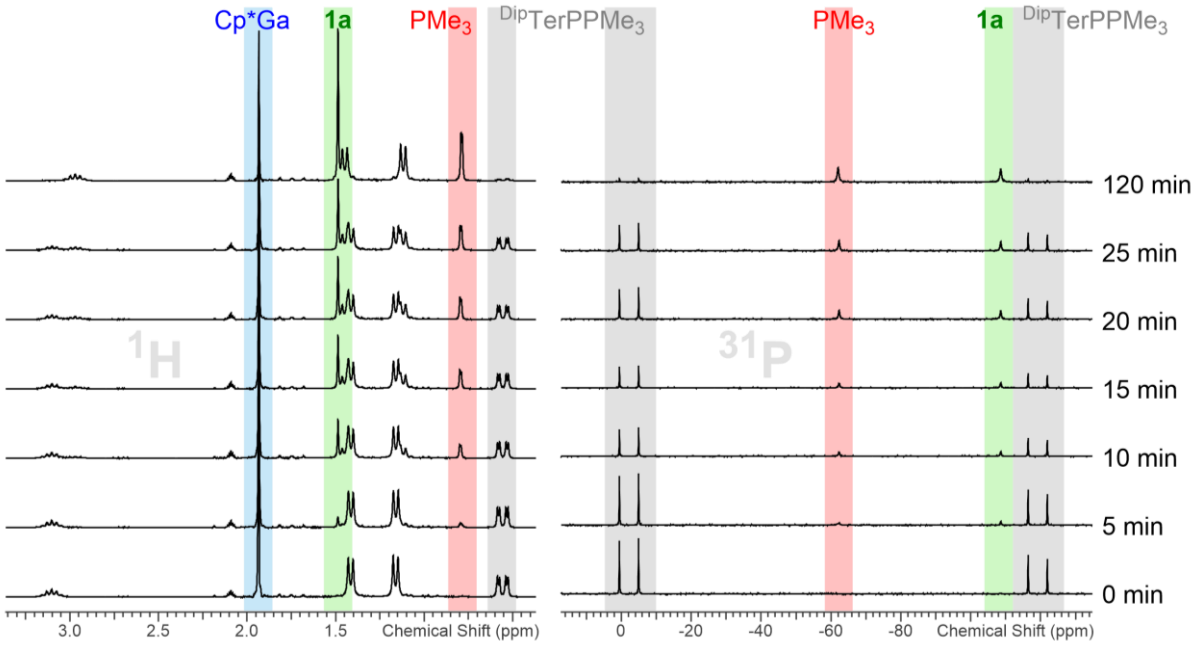

Figure S26: In situ ^{1}H (left) and $^{31}P\{^{1}H\}$ (right) NMR spectra of the thermal cleavage of **^{Dip}TerP=GaCp*** (**1a**) in the presence of **PMe_3** at +15 °C.

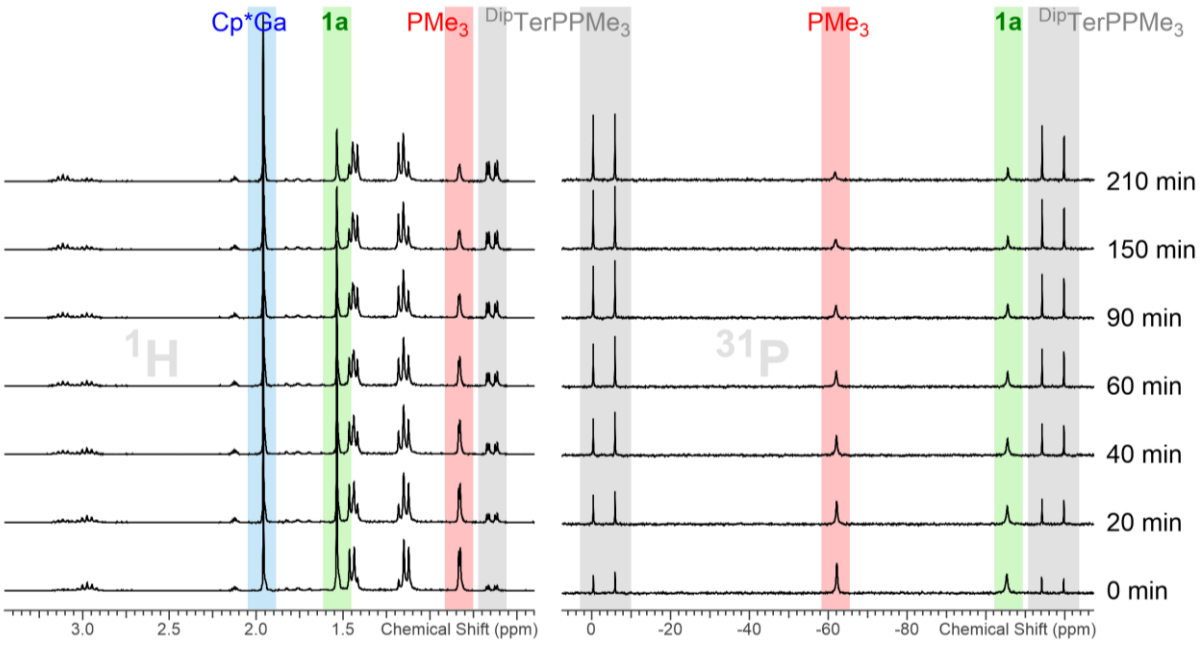

Figure S27: Concentration profile of the photoreaction of **^{Dip}TerP(PMe_3)** with **Cp*Ga** at −10 °C.

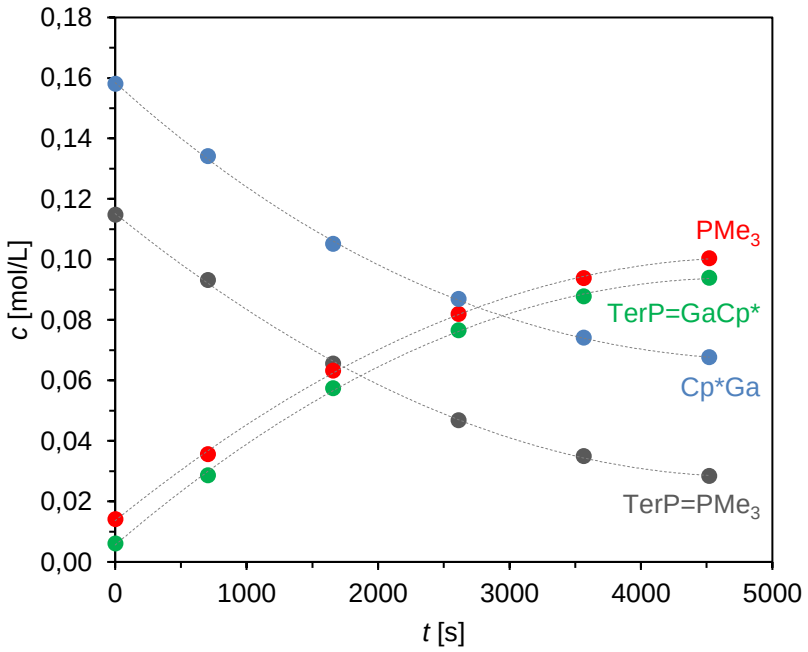

Figure S28: Concentration profile of the thermal cleavage of **^{Dip}TerP=GaCp*** (**1a**) in the presence of **PMe_3** at +10 °C. Fit curves according to models **i** (left) and **ii** (right).

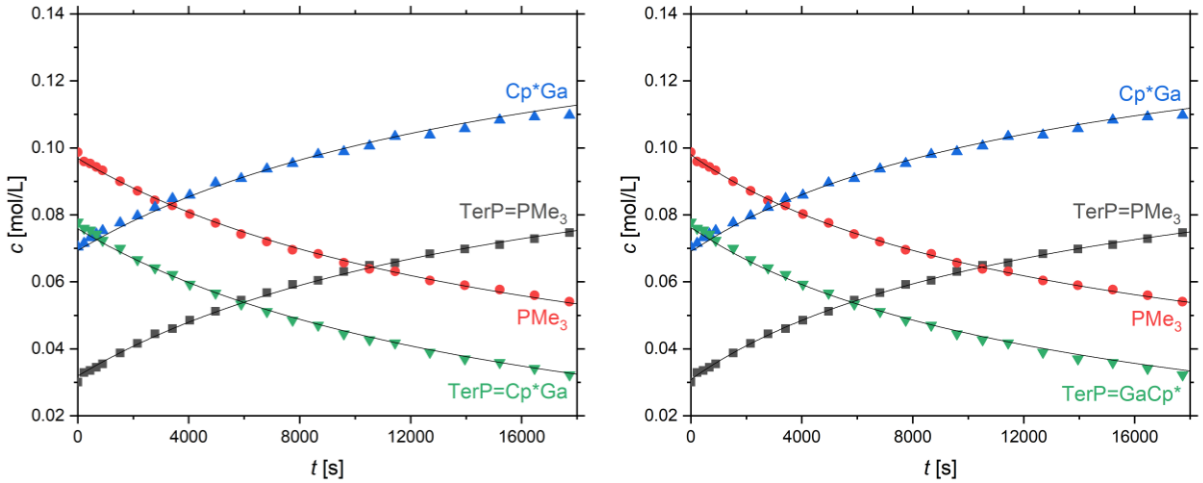

Figure S29: Concentration profile of the thermal cleavage of **^{Dip}TerP=GaCp*** (**1a**) in the presence of **PMe_3** at +15 °C. Fit curves according to models **i** (left) and **ii** (right).

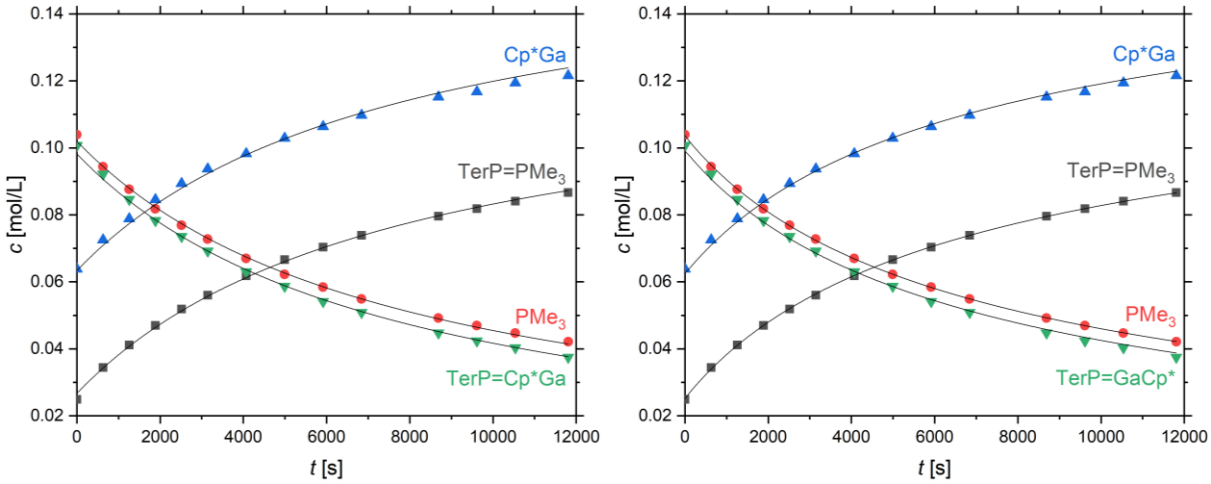

Figure S30: Concentration profile of the thermal cleavage of **^{Dip}TerP=GaCp*** (**1a**) in the presence of **PMe_3** at +20 °C. Fit curves according to models **i** (left) and **ii** (right).

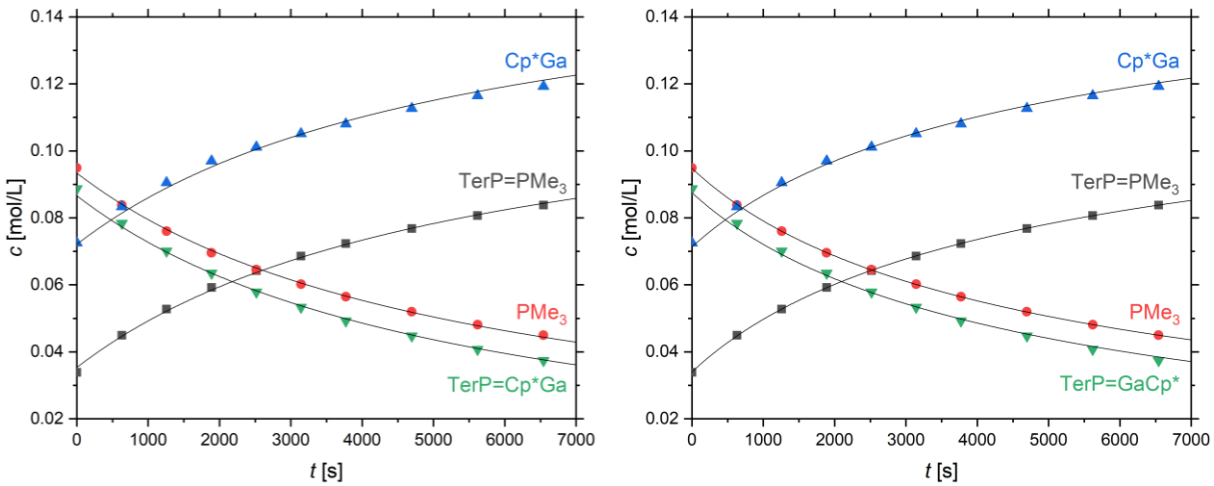

Figure S31: Concentration profile of the thermal cleavage of **^{Dip}TerP=GaCp*** (**1a**) in the presence of **PMe_3** at +25 °C. Fit curves according to models **i** (left) and **ii** (right).

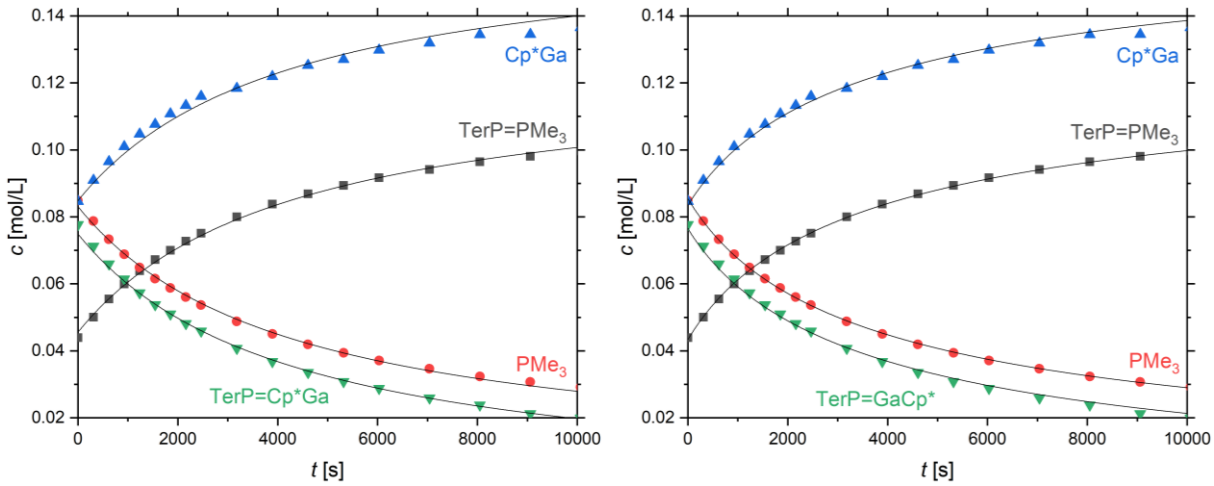

The kinetics of the thermal reactions were evaluated using a non-linear fitting procedure. Two conceivable reaction mechanisms were considered: (**i**) a second order reaction involving the direct reaction between **1a** and PMe_3 and (**ii**) a dissociative process where **1a** fragments into the phosphinidene ^{Dip}TerP and Cp*Ga in the first step, followed by a reaction between ^{Dip}TerP and PMe_3 to form ^{Dip}TerP=PMe_3. In general, both models give reasonable fits. The residual sums of squares as well as the R^2 values

imply a slightly better fit in case of model **ii** (Table S6). However, the differences are subtle, and the improved fit can likely be attributed to the additional number of parameters in model **ii**.

Table S6. Summary of the fits.

		10 °C	15 °C	20 °C	25 °C
Residual	Model **i**	8.46×10^{-5}	4.81×10^{-5}	3.52×10^{-5}	1.02×10^{-4}
	Model **ii**	6.09×10^{-5}	2.55×10^{-5}	1.77×10^{-5}	4.74×10^{-5}
R^2	Model **i**	0.99799	0.99837	0.99848	0.99857
	Model **ii**	0.99856	0.99913	0.99922	0.99933

The experimental data were fitted using the following differential rate laws:

*Model **i***

$$\frac{d[\mathbf{1a}]}{dt} = \frac{d[\mathrm{PMe_3}]}{dt} = -k[\mathbf{1a}][\mathrm{PMe_3}]$$

$$\frac{d[\mathrm{TerPPMe_3}]}{dt} = \frac{d[\mathrm{Cp^*Ga}]}{dt} = +k[\mathbf{1a}][\mathrm{PMe_3}]$$

The terms in square brackets indicate the concentration of the respective species in solution. The model has five parameters, namely the initial concentrations of the four substances as well as the rate constant k.

*Model **ii***

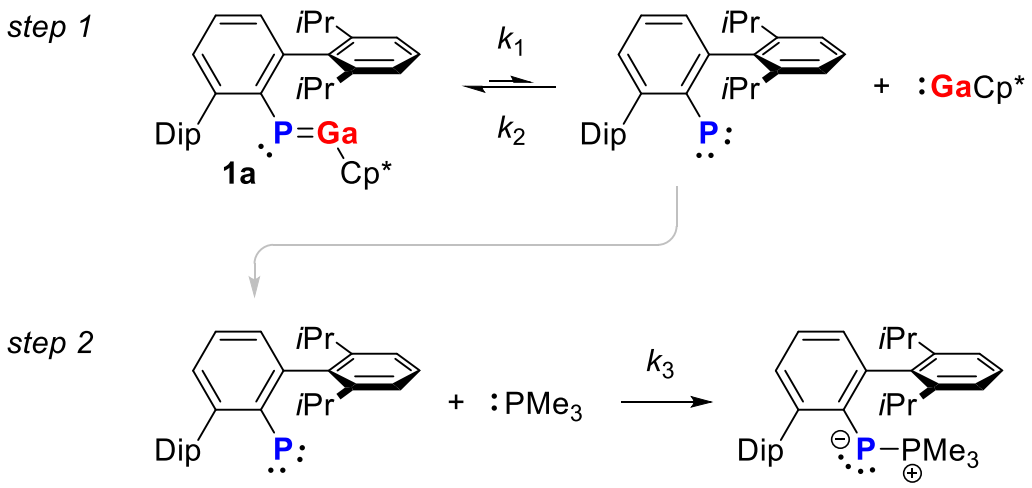

$$\frac{d[\mathbf{1a}]}{dt} = -k_1[\mathbf{1a}] + k_2[\mathrm{TerP}][\mathrm{Cp^*Ga}]$$

$$\frac{d[\mathrm{Cp^*Ga}]}{dt} = +k_1[\mathbf{1a}] - k_2[\mathrm{TerP}][\mathrm{Cp^*Ga}]$$

$$\frac{d[\mathrm{TerP}]}{dt} = +k_1[\mathbf{1a}] - k_2[\mathrm{TerP}][\mathrm{Cp^*Ga}] - k_3[\mathrm{TerP}][\mathrm{PMe_3}]$$

$$\frac{d[\mathrm{PMe_3}]}{dt} = -k_3[\mathrm{TerP}][\mathrm{PMe_3}]$$

$$\frac{d[\mathrm{TerPPMe_3}]}{dt} = +k_3[\mathrm{TerP}][\mathrm{PMe_3}]$$

Again, the terms in square brackets indicate the concentration of the different species. This second model has eight parameters: the initial concentrations of all five species, as well as the rate constants k_1, k_2, and k_3.

As the proposed phosphinidene $^{\mathrm{Dip}}$TerP would be a highly reactive transient species, its concentration is expected be very low throughout the reaction. Unsurprisingly, it could not be detected by NMR methods. Its concentration was therefore restrained during the fit (steady state approximation), however including a high uncertainty.

Non-linear fitting of the ordinary differential equations (ODE) was performed using the program *Origin*, analogously to the procedure outlined in a previous publication.[8] The obtained rate constants were then used to estimate the enthalpy and entropy of activation, $\Delta H^{\ddagger}$ and $\Delta S^{\ddagger}$, according to the Eyring equation:

$$k = \kappa \frac{k_B T}{h} \exp\left(-\frac{\Delta G^{\ddagger}}{RT}\right)$$

$$\ln\left(\frac{k}{T}\right) = -\frac{\Delta H^{\ddagger}}{R} \cdot \frac{1}{T} + \frac{\Delta S^{\ddagger}}{R} + \ln\left(\frac{k_B}{h}\right)$$

The transmission coefficient κ is assumed to be unity in the second equation. The linearized Eyring plots for both models are depicted in Figure S32.

Figure S32: Temperature dependence of the rate constant(s) of the thermal cleavage of **^{Dip}TerP=GaCp*** (**1a**) in the presence of **PMe_3** according to model **i** (left) and **ii** (right).

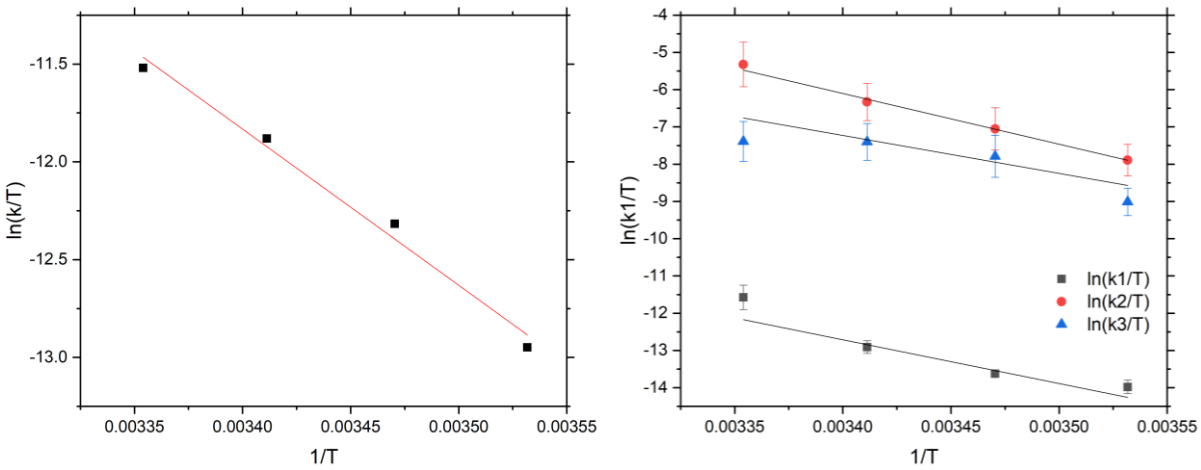

Table S7 summarizes the derived activation energies for both models.

Table S7. Summary of the activation energies according to models **i** and **ii**.

Model	Rate constant	$\Delta H^{\ddagger}$ [kJ·mol^{-1}]	$\Delta S^{\ddagger}$ [J·mol^{-1}·K^{-1}]	$\Delta G^{\ddagger}_{25\,°C}$ [kJ·mol^{-1}]
i	k	+68±6	−63±21	+87±12
ii	k_1	+98±26	+29±90	+89±53
	k_2	+113±6	+137±22	+72±13
	k_3	+85±36	+30±123	+76±72

Clearly, the error margins of model **ii** are larger, which can be attributed to a large interdependency of the three rate constants in the non-linear fit. This can be an indicator of overparameterization; however, this kind of dependency of the constants may also to be expected if the reaction follows pseudo-2nd order kinetics due to the low concentration of the intermediate ^{Dip}TerP. Yet, the activation barrier associated with k_2 is surprisingly large for the proposed association of Cp*Ga and ^{Dip}TerP, and especially we would expect a small enthalpic but a large, negative entropic term for such a process. Similar considerations hold true for the reaction associated with k_3, *i.e.*, the association of ^{Dip}TerP and PMe_3. Model **i**, on the other hand, shows the expected behaviour of the enthalpic and entropic contributions.

To further validate the mechanism, we recorded additional data at 25 °C using isolated **1a** and an excess of PMe_3 (5 equivalents, Figure S33). Again, both models can be fitted against the data. Within the error margin, model **i** yielded a rate constant (k = 0.0027(2) L mol^{-1} s^{-1}) that is equal to the rate constant obtained from the experiment with a 1:1 ratio of **1a** and PMe_3 (k = 0.00296(4) L mol^{-1} s^{-1}), as expected for a second-order reaction. The rate constants of model **ii** were associated with high uncertainties (k_1 = 0.036(17) s^{-1}, k_2 = 3.6(1.7) L mol^{-1} s^{-1}, k_3 = 0.03(3) L mol^{-1} s^{-1}), and while technically not significantly different from the values of the experiment with a 1:1 ratio within a 3 σ interval (k_1 = 0.0028(9) s^{-1}, k_2 = 1.5(9) L mol^{-1} s^{-1}, k_3 = 0.18(10) L mol^{-1} s^{-1}), the large errors make any reasonable comparison impossible. Seeing that some of the constants differ by an order of magnitude, we think that model **ii** is less likely to correctly describe the reaction kinetics.

Figure S33: Concentration profile of the thermal cleavage of **^{Dip}TerP=GaCp*** (**1a**) in the presence of **PMe_3** (5 equiv.) at +25 °C. Fit curves according to models **i** (left) and **ii** (right).

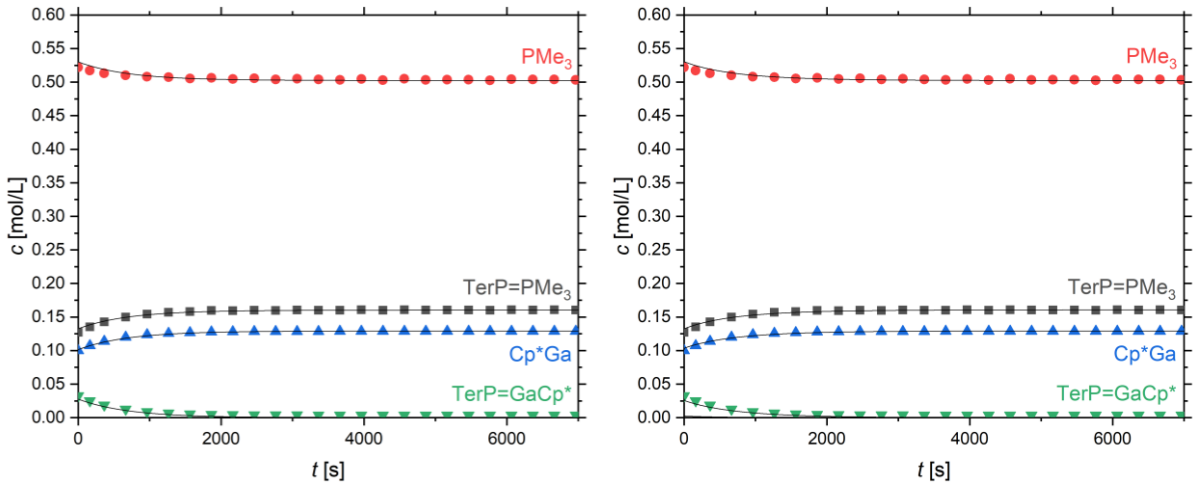

5 Computational details

5.1 General remarks

Computations were carried out using ORCA 5.0.3,[9] Gaussian09,[10] xTB 6.5.1,[11] NBO 6.0,[12] and MultiWfn 3.7.[13]

DFT structure optimizations using analytic gradients were performed using ORCA and employed the hybrid exchange-correlation functional B3LYP[14] (using VWN5[14a] for the local correlation term) in conjunction with Grimme's dispersion correction D3(BJ)[15] and the def2-TZVP basis set[16] (notation B3LYP-D3/def2-TZVP). The resolution-of-identity (RI) approximation was applied, using Weigend's accurate Coulomb-fitting basis set (def2/J).[17] Numerical integration of the exchange-correlation energy was done on ORCA's default XC grid ("DefGrid2"). The exact exchange term of the hybrid functional B3LYP was approximated by the Chain Of Spheres approximation (COSX),[18] using the default COSX grid ("DefGrid2") for numerical integration. All structures were fully optimized and confirmed as minima or transition states by analytic frequency analyses.

Calculated frequencies were scaled by 0.960 (as derived from Truhlar's Reduced Scale Factor Optimization model).[19]

Chemical shifts and **coupling constants** were derived by the GIAO method[20] at the PBE0[21]-D3/def2-TZVP level of theory (using the B3LYP-D3/def2-TZVP geometries, *vide supra*) using Gaussian09. Calculated absolute ^{1}H NMR shifts ($\sigma_{calcd,X}$) were referenced to the calculated absolute shift of tetramethylsilane ($\sigma_{calcd,TMS}$):

$$\delta_{calc,X} = \sigma_{calcd,TMS} - \sigma_{calcd,TMS}$$

At the PBE0-D3/def2-TZVP level of theory, $\sigma_{calcd,TMS}$ amounts to +31.75 ppm.

Calculated absolute ^{31}P NMR shifts ($\sigma_{calcd,X}$) were referenced to the experimental absolute shift of 85% H_3PO_4 in the gas phase ($\sigma_{ref,1}$ = 328.35 ppm),[22] using PH_3 ($\sigma_{ref,2}$ = 594.45 ppm) as a secondary standard:[23]

$$\begin{aligned} \delta_{calc,X} &= (\sigma_{ref,1} - \sigma_{ref,2}) - (\sigma_{calcd,X} - \sigma_{calcd,PH_3}) \\ &= \sigma_{calcd,PH_3} - \sigma_{calcd,X} - 266.1 \text{ ppm} \end{aligned}$$

At the PBE0-D3/def2-TZVP level of theory, σ_{calcd,PH_3} amounts to +572.04 ppm.

UV-vis absorption spectra were calculated with Gaussian09 using the TD-DFT method[24] at the B3LYP-D3/cc-pVTZ[25] level of theory (using the B3LYP-D3/def2-TZVP geometries, *vide supra*).

NBO analyses were performed using the B3LYP-D3/def2-TZVP densities. Reported partial charges refer to the Natural Charges. **ELF**[26] and **AIM**[27] analyses were performed using MultiWfn.

Reaction paths were investigated using a combination of relaxed potential energy surface scans, the nudged elastic band (NEB) method,[28] as well as transition state searches using the eigenvector-following method.[29] Additionally, xTB's meta-dynamics[30] reaction path finder was used for fast sampling of the potential energy surface, using the GFN2-xTB method.[31] All relevant transition states were eventually optimized at the B3LYP-D3/def2-TZVP level of theory as outlined above.

Please note that all computations were carried out for single, isolated molecules in the gas phase (ideal gas approximation). There may well be significant differences between gas phase and condensed phase.

Table S8. Summary of calculated data (B3LYP-D3/def2-TZVP). All energies in atomic units.

Compound	PG	N_{imag}	$\langle S^2 \rangle$	E_{tot}	U_0	U_{298}	H_{298}	G_{298}
Cp*Ga	C_{5v}	0		−2314.8255	−2314.6054	−2314.5911	−2314.5902	−2314.6437
^{Dip}TerPPMe$_3$	C_1	0		−1967.6729	−1966.9686	−1966.9289	−1966.9279	−1967.0320
PMe$_3$	C_{3v}	0		−461.0431	−460.9310	−460.9243	−460.9234	−460.9592
1a	C_1	0		−3821.4383	−3820.6287	−3820.5802	−3820.5792	−3820.7027
1b	C_1	0		−4057.2727	−4056.2949	−4056.2375	−4056.2366	−4056.3769
2a	C_1	0		−1506.6360	−1506.0466	−1506.0150	−1506.0140	−1506.1026
1a·PMe$_3$	C_1	0		−4282.5046	−4281.5790	−4281.5232	−4281.5223	−4281.6584
1a···PMe$_3$ (vdW)	C_1	0		−4282.4935	−4281.5699	−4281.5130	−4281.5121	−4281.6509
^{Dip}TerPPMe$_3$·GaCp*	C_1	0		−4282.5155	−4281.5906	−4281.5345	−4281.5335	−4281.6707
^{Dip}TerP (S)	C_{2v}	0	1.02	−1506.5597	−1505.9724	−1505.9395	−1505.9386	−1506.0300
^{Dip}TerP (T)	C_{2v}	0	2.02	−1506.5683	−1505.9809	−1505.9480	−1505.9471	−1506.0395
TS1	C_1	1		−4282.4583	−4281.5337	−4281.4784	−4281.4774	−4281.6122
TS2	C_1	1		−4282.4731	−4281.5490	−4281.4935	−4281.4925	−4281.6284

5.2 Calculated UV-vis absorption data

UV-vis absorption spectra were calculated at the TD-DFT/B3LYP-D3/cc-pVTZ level of theory, using the structures optimized at the B3LYP-D3/def2-TZVP level of theory.

Table S9. Calculated electronic excitations of **Cp*Ga** (B3LYP-D3/cc-pVTZ).

State	Symmetry	λ [nm]	Oscillator strength	Main excitation
S1	$^1A_2$	277	0.0000	π→LV(Ga)
S2	$^1E_2$	274	0.0000	π→LV(Ga)
S3	$^1A_1$	241	0.0908	π→LV(Ga)
S4	$^1E_1$	223	0.0239	π→LV(Ga)

Table S10. Calculated electronic excitations of **^{Dip}TerPPMe$_3$** (B3LYP-D3/cc-pVTZ).

State	Symmetry	λ [nm]	Oscillator strength	Main excitation
S1	^1A	410	0.0258	HOMO→LUMO
S2	^1A	369	0.0330	HOMO→LUMO+1
S3	^1A	338	0.0286	HOMO→LUMO+2

Figure S34. Relevant Kohn-Sham orbitals of **^{Dip}TerPPMe$_3$** (B3LYP-D3/cc-pVTZ, isovalue = 0.05).

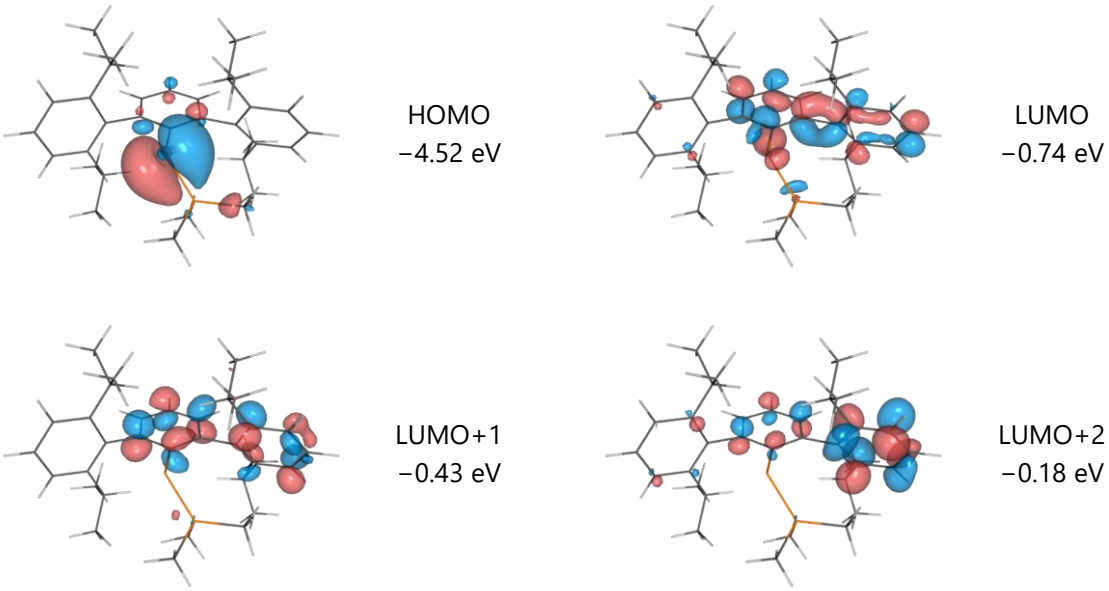

Table S11. Calculated electronic excitations of **1a** (B3LYP-D3/cc-pVTZ).

State	Symmetry	λ [nm]	Oscillator strength	Main excitation
S1	^1A	635	0.0022	HOMO→LUMO
S2	^1A	423	0.0127	HOMO→LUMO+1
S3	^1A	417	0.0005	HOMO→LUMO+2
S4	^1A	366	0.0859	HOMO→LUMO+3

Figure S35. Relevant Kohn-Sham orbitals of **1a** (B3LYP-D3/cc-pVTZ, isovalue = 0.05).

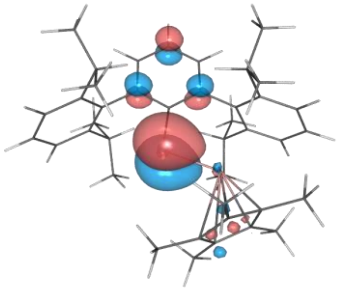

HOMO
−4.38 eV

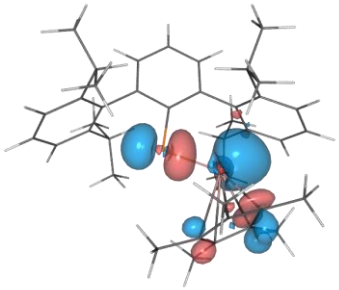

LUMO
−1.50 eV

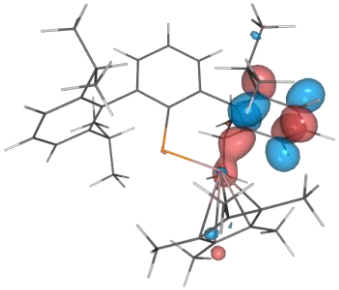

LUMO+1
−0.81 eV

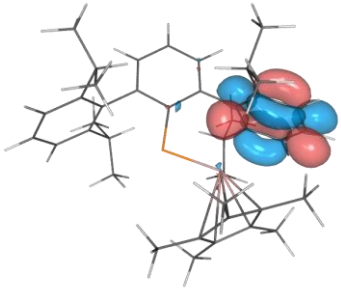

LUMO+2
−0.71 eV

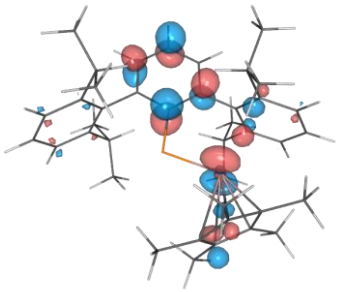

LUMO+3
−0.41

Table S12. Calculated electronic excitations of **1b** (B3LYP-D3/cc-pVTZ).

State	Symmetry	λ [nm]	Oscillator strength	Main excitation
S1	^1A	623	0.0021	HOMO→LUMO
S2	^1A	429	0.0166	HOMO→LUMO+1
S3	^1A	411	0.0012	HOMO→LUMO+2
S4	^1A	366	0.0762	HOMO→LUMO+3

Figure S36. Relevant Kohn-Sham orbitals of **1b** (B3LYP-D3/cc-pVTZ, isovalue = 0.05).

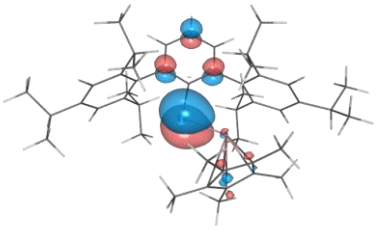

HOMO
−4.34 eV

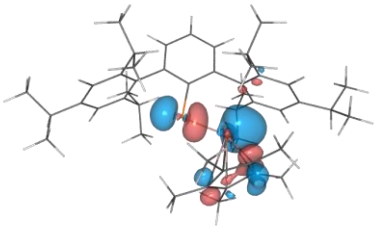

LUMO
−1.46 eV

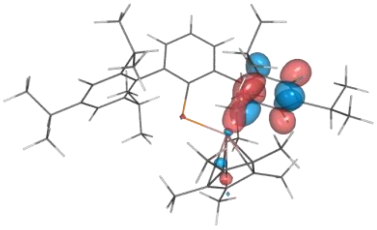

LUMO+1
−0.82 eV

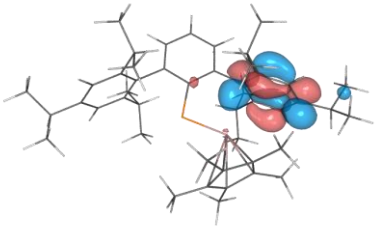

LUMO+2
−0.63 eV

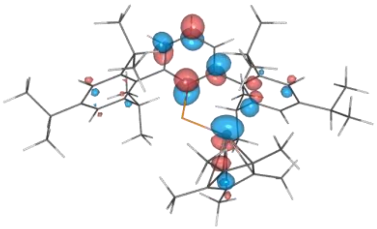

LUMO+3
−0.36

5.3 Calculated NMR data

NMR data were calculated at the PBE0-D3/def2-TZVP level of theory, using the structures optimized at the B3LYP-D3/def2-TZVP level of theory.

Table S13. Calculated NMR shifts and coupling constants at PBE0-D3/def2-TZVP. Experimental values given in brackets.

Compound	Nucleus	Group	# nuc.	Mult.	δ [ppm]	J [Hz]
^{Dip}TerPPMe$_3$	^{1}H	P*Me$_3$*	9	dd	+0.81 (+0.75)	[a]
	^{31}P	^{Dip}Ter*P*	1	d	−134.2 (−116.1)	−546 (−563)
		*P*Me$_3$	1	d	+4.7 (−3.4)	−546 (−563)
^{Dip}TerPGaCp* (**1a**)	^{1}H	Ga*Cp**	15	s	+1.62 (+1.50)	
	^{31}P	^{Dip}Ter*P*	1	s	−105.2 (−105.5)	
^{Tip}TerPGaCp* (**1b**)	^{1}H	Ga*Cp**	15	s	+1.61 (+1.53)	
	^{31}P	^{Tip}Ter*P*	1	s	−107.9 (−109.8)	
PMe$_3$	^{1}H	P*Me$_3$*	9	br s	+0.97 (+0.91)	
	^{31}P	*P*Me$_3$	1	s	−59.3 (−62.0)	
Cp*Ga	^{1}H	*Cp**	15	s	+2.00 (+2.05)	

[a] not computed

5.4 Electronic structure

NBO/NLMO analysis. According to NBO analysis of ^{Dip}TerPGaCp* (**1a**), the P–Ga interaction can be understood as a highly polarized double bond. While the σ-type NBO is evenly distributed between the two elements (P: 51%, Ga: 49%), the π-type NBO is mainly localized at the P atom (P: 87%, Ga: 13%). The P-Ga σ bond is essentially formed through the interaction of the 3p_x orbital at P with the 4*s* orbital at Ga, whereas the π bond is formed by the interaction of the p_z orbitals at both atoms. The LP at P has mainly 3*s* character. The corresponding NLMOs (which include delocalization effects on the NBOs) are depicted in Figure S37.

Figure S37. Selected NLMOs of ^{Dip}TerPGaCp* (**1a**, B3LYP-D3/def2-TZVP, isovalue = 0.04).

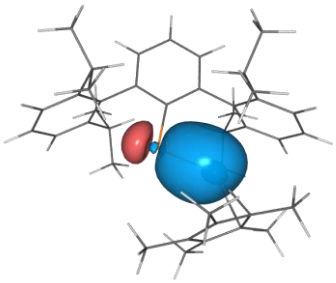

σ(P-Ga)
−12.5 eV
P: 50%
(s: 8%, p: 91%)
Ga: 48%
(s: 94%, p: 5%)

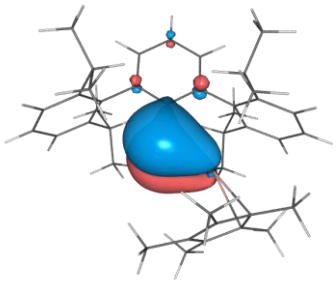

π(P-Ga)
−5.2 eV
P: 78%
(s: 0%, p: 100%)
Ga: 11%
(s: 0%, p: 99%)
i-C: 4%
(s: 0%, p: 99%)

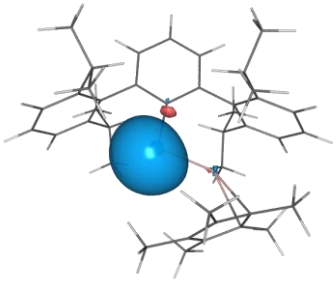

LP(P)
−15.2 eV
P: 92%
(s: 76%, p: 24%)
Ga: 7%
(s: 2%, p: 98%)

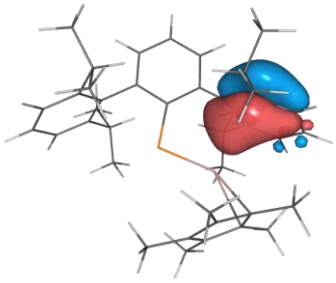

π(Dip)
−9.0 eV
∑ C: 97%
Ga: 1%
(s: 16%, p: 83%)

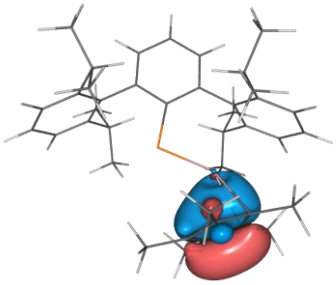

π(Cp*)
−9.4 eV
∑ C: 93%
Ga: 4%
(s: 20%, p: 80%)

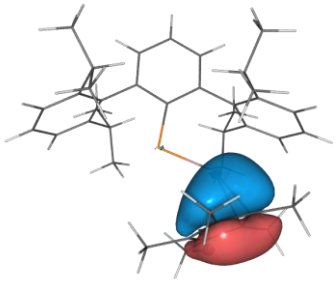

π(Cp*)
−10.6 eV
∑ C: 89%
Ga: 7%
(s: 47%, p: 53%)

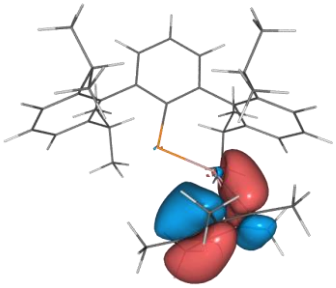

π(Cp*)
−7.5 eV
∑ C: 88%
Ga: 7%
(s: 42%, p: 58%)

The Ga atom possesses two lone valences (LVs, 4p_x and 4p_y orbitals), which are stabilized by intramolecular donor-acceptor interactions from the phosphorus lone pair (LP(P)→p_x(Ga): 299 kJ/mol), as well as the π bonding systems of the Cp* ligand (π(Cp*)→p_x(Ga): 69 kJ/mol, π(Cp*)→p_y(Ga): 175 kJ/mol, total: 244 kJ/mol) and one of the flanking Dip groups (π(Dip)→p_x(Ga): 14 kJ/mol, π(Dip)→p_y(Ga): 17 kJ/mol, total:

31 kJ/mol, see also Figure S37). Further significant stabilization can also be traced back to the C-C σ-bonding system of the Cp* ligand (incl. the C-Me bonds), amounting to a total of 470 kJ/mol.

Natural charges. The polarized nature of the P=Ga double bond is corroborated by natural population analysis, with a positively charged Ga atom (+1.11) and a negatively charged P atom (−0.28). The total natural charge of the Cp* ligand amounts to −0.43, *i.e.*, there is a significant charge transfer of 0.57 electrons from the Cp^{*-} moiety to the formal $TerPGa^{+}$ fragment.

Bond orders. The P–Ga bond is characterized by a Wiberg bond index of 1.31 (*cf.* Table S14), *i.e.*, it has significant double bond character. The P–C bond order of 1.07 indicates some delocalization of the P–Ga π bond into the ^{Dip}Ter substituent. All individual Ga–C bond orders are low (<0.3). The two closest C–Ga contacts to the Cp* ligand show slightly higher bond orders (0.18, 0.27) than the other three C atoms (~0.10). The total Ga–Cp* bond order (summed over the five ring atoms) amounts to 0.74. The bond orders to the C atoms of the Dip group are all below 0.05 (sum: 0.12), in agreement with the low donor-acceptor energies between the Dip group and the LVs at the Ga atom.

Table S14. Selected Wiberg bond indices of **1a**. Atom numbering according to the XYZ file.

			Ter	Dip						Cp*				
	P	Ga	*i*-C	*i*-C	*o*-C	*o*-C′	*m*-C	*m*-C′	*p*-C	C	C	C	C	C
	1	2	3	41	42	49	43	47	45	70	71	72	73	74
P	–	1.31	1.07	0.01	0.01	0.01	0.00	0.01	0.01	0.05	0.01	0.02	0.01	0.09
Ga	1.31	–	0.02	0.04	0.02	0.01	0.00	0.01	0.03	0.18	0.09	0.10	0.10	0.27

Lewis representation. On the basis of the above considerations, we propose the Lewis resonance scheme shown in Scheme S1. The structures in the centre (**II-a** or **II-b**) best represent the charge distribution and bonding situation in a single structure, however all structures are needed for a complete picture. The polarization of the Ga=P double

bond is reflected in the resonance to the structures of type **III**. Due to the donor-acceptor interaction between the LP at the P atom and the empty 4p_x orbital at the Ga atom, the P–Ga bond could also be understood as a non-classical, highly polarized triple bond. Nonetheless, we attribute only a small weight to the leftmost resonance structures (type **I**), considering the computed partial charges and bond orders. A simplified bonding scheme illustrating the involved orbitals is shown in Scheme S2.

Scheme S1. Lewis resonance scheme of **1a** as derived from NBO analysis.

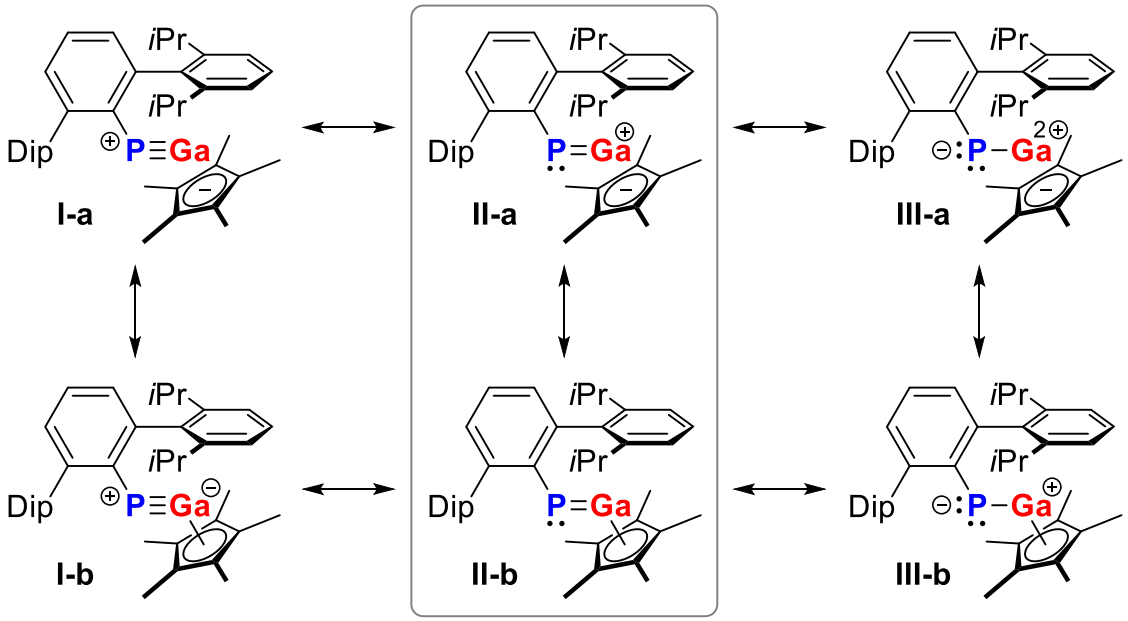

Scheme S2. Simplified bonding scheme of **1a** according to NBO analysis. The polarized P–Ga π bond is formed by the p_z orbitals (black). An additional stabilizing interaction is found between the LP at P and the empty p_x orbital at Ga (blue), which is, however, not a classical π bonding interaction. The empty p_y orbital at Ga is mainly stabilized by the Cp* ligand. The P–Ga σ bond is formed by a p(P)-s(Ga) interaction (not depicted).

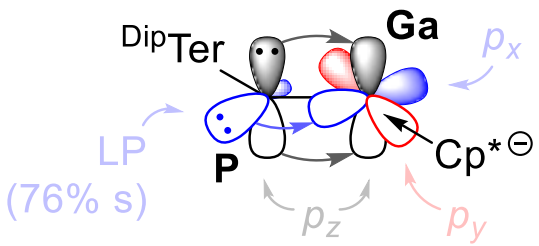

Electron Localization function. The ELF plotted in the Ga–P–C plane (Figure S38, left) nicely shows the presence of the LP at the P atom (red maximum on the lower left of the P atom) as well as the P–Ga and P–C bonds (maxima along the P–Ga/P–C axes). The ELF plotted along the P–Ga axis, but perpendicular to the Ga−P−C plane (Figure S38, right) reveals that the π electron density is strongly localized towards P, in line with the resonance between Lewis structures **II** and **III**.

Figure S38. ELF of **1a** in the Ga−P−C plane (left) and perpendicular to that plane (right).

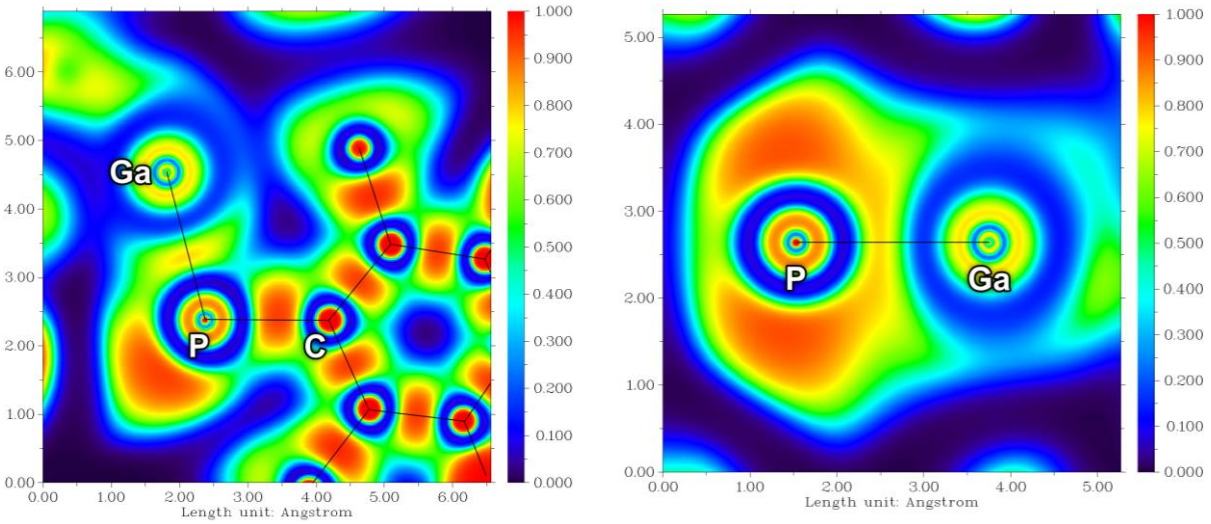

AIM analysis. Like the ELF, the Laplacian of the electron density $\nabla^2\rho$ in the Ga–P–C plane (Figure S39, left) indicates a LP at the P atom that points away from the C and Ga atoms. There is only a single valence shell charge concentration (VSCC) along the P–Ga bond, which is shifted towards the P atom, indicating a strongly polarized interaction with ionic character (see also Figure S40a). The Laplacian plot along the P–Ga bond in the p_z plane (Figure S39, right) corroborates the charge accumulation near the P atom in the π bonding system, in agreement with the NBO and ELF results. The ellipticity ε at the bond critical point (BCP) of 0.31 indicates double bond character (cf. ~0.3 for ethylene, ~0.2 for benzene;[32] Table S15).

The plot of $\nabla^2\rho$ along the P–C bond path (Figure S40b) indicates a typical polarized covalent bond, with two VSCCs. The electron density ρ at the bond critical point (BCP)

amounts to 0.154 a.u., also indicative of a covalent interaction (Table S15).[33] Its ellipticity of 0.37 hints at double bond character, in line with the delocalization of the π(P–Ga) NLMO (*vide supra*).

Notably, there is a bond path between the Ga atom and the nearest C atom of the Cp* moiety (Figure S39, left; note that the path leaves the projection plane after the BCP). A second Ga···C bond path is found towards the *ipso*-C of the flanking Dip group. The positive values of $\nabla^2\rho$ at the BCP (Figure S40c-d, Table S15) are indicative of closed-shell (electrostatic) interactions, which is corroborated by the rather low electron density ρ at the BCP, especially in case of the Ga···C_{Dip} interaction. The slightly negative values of the energy density $H(r)$ may be attributed to the weak dative character revealed by the NBO analysis.

The bond path that leads from the P atom to the left (see left panel of Figure S39) is due to a van-der-Waals interaction with the Cp* moiety.

Figure S39. Contour plot of the Laplacian of the electron density $\nabla^2\rho$ of **1a** in the Ga–P–C plane (left) and perpendicular to that plane (right). Solid lines correspond to positive values (charge depletion), dashed lines correspond to negative values (charge accumulation). The plot is overlaid with the results of the topological analysis of the electron density ρ. Brown: maxima in the electron density (*i.e.*, the positions of the nuclei), blue: bond critical points, yellow: ring critical points; grey lines: "bond" paths.

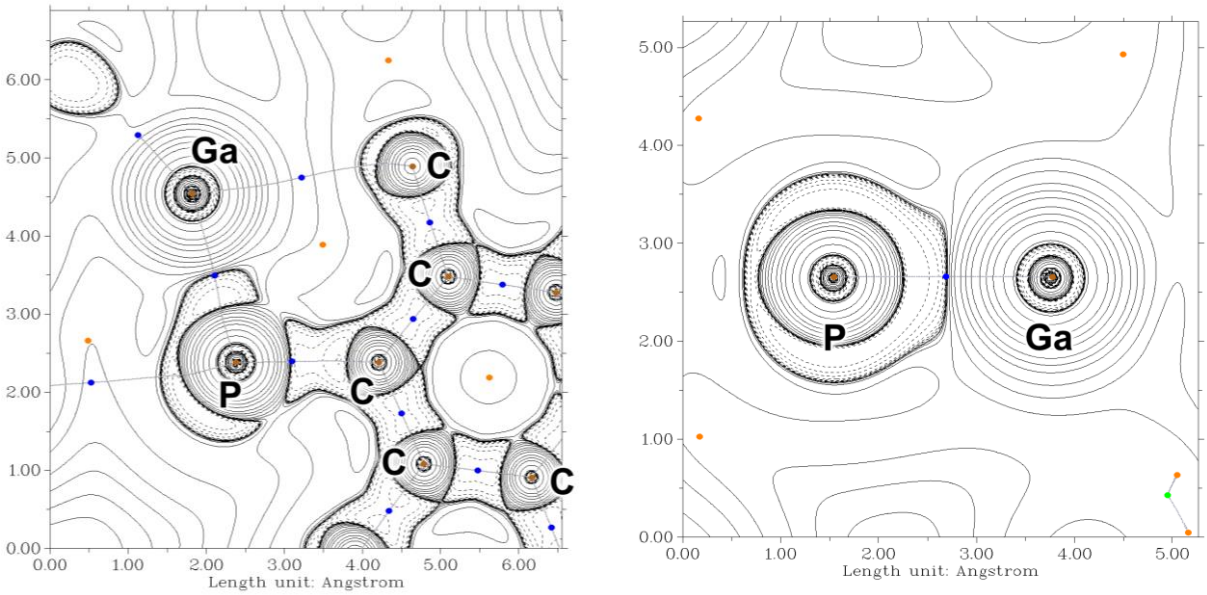

Figure S40. Plots of the Laplacian $\nabla^2\rho$ of the electron density of **1a** along the (a) P–Ga, (b) P–C, (c) Ga···C_{Cp^*}, and (d) Ga···C_{Dip} bond paths. The bond critical points (BCPs) are set to d = 0.

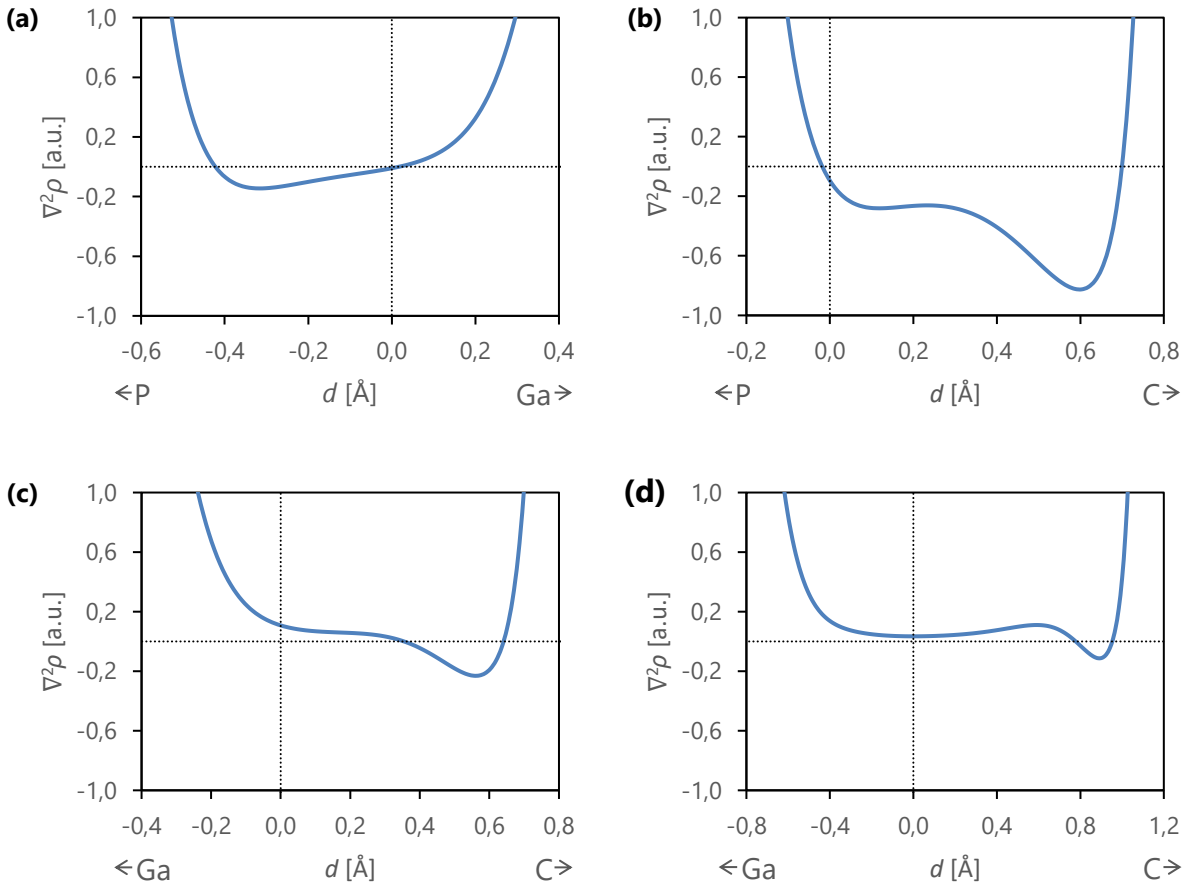

Table S15. Topological properties at the BCP of selected interactions in **1a** (ρ: electron density, $\nabla^2\rho$: Laplacian of the electron density, H(r): total energy density, ε: ellipticity).

Interaction	ρ [a.u.]	$\nabla^2\rho$ [a.u.]	H(r) [a.u.]	ε
P–Ga	0.091	−0.010	−0.040	0.310
P–C	0.154	−0.095	−0.146	0.370
Ga···C_{Cp^*}	0.075	+0.108	−0.025	(0.738)
Ga···C_{Dip}	0.020	+0.034	−0.001	(0.601)

5.5 Reaction path

Our calculations revealed that the (thermal) formation of **1a** is endergonic ($\Delta G°$ = +36.2 kJ/mol; Figure S41), which explains that no reaction between ^{Dip}TerPPMe$_3$ and Cp*Ga is observed under thermal regime. Conversely, this also means that the

thermal reverse reaction is expected to be quantitative, in agreement with experimental observation.

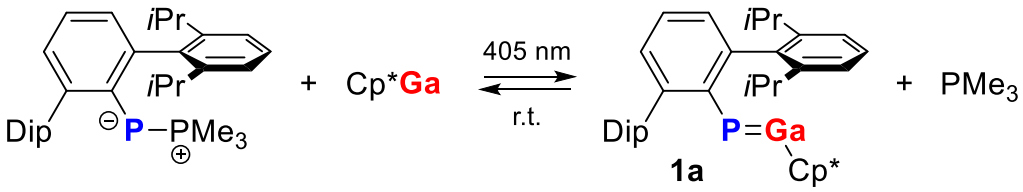

To obtain a rough idea of the reactivity of ^{Dip}TerPPMe$_3$ in its first excited state (S1), a scan of the P–P bond was performed, revealing a very flat potential for its dissociation in the S1 state. We assume that upon dissociation, the excited molecules deactivate either through a conical intersection leading to PMe$_3$ and singlet ^{Dip}TerP, or *via* intersystem crossing to PMe$_3$ and triplet ^{Dip}TerP. The highly reactive phosphinidene then reacts with Cp*Ga to the final product **1a**. A detailed investigation of these dynamics was, however, outside the scope of the present study and will be further pursued in the future.

Next, we investigated the thermal reverse reaction of PMe$_3$ with **1a** (cf. section 4.2, "Kinetic studies using NMR spectroscopy") to obtain a better understanding of the reaction mechanism. As depicted in Figure S41, we located two different reaction paths which are characterized by transition states **TS1** and **TS2**. The former path is accessed *via* formation of a weak donor-acceptor complex between PMe$_3$ and **1a** followed by rearrangement of the PMe$_3$ group, whereas the latter can be regarded as a nucleophilic attack of PMe$_3$ at the P atom of **1a** (S_N2-type mechanism). While **TS1** is associated with a rather large activation barrier of $\Delta G^{\ddagger}$ = 121.4 kJ/mol, **TS2** is in the expected energetic range ($\Delta G^{\ddagger}$ = 80.1 kJ/mol, cf. $\Delta G^{\ddagger}_{exptl.}$ = 87±12 kJ/mol for model **i**), rendering this a likely mechanism for the reverse reaction.

Dissociation of **1a** leads to the formation of Cp*Ga and the highly reactive phosphinidene ^{Dip}TerP, which is expected to possess a triplet ground state with a singlet-triplet gap of 45.5 kJ/mol according to broken-symmetry UB3LYP-D3/def2-TZVP calculations using the spin decontamination[34] proposed by Malrieu:[35]

$$E_S - E_T = \frac{\langle S^2 \rangle_T}{\langle S^2 \rangle_T - \langle S^2 \rangle_{BS}} \cdot (E_{BS} - E_T)$$

E_S, E_T, and E_{BS} are the energies of the "true" singlet state, triplet state, and broken-symmetry solution, respectively. $\langle S^2 \rangle_T$, and $\langle S^2 \rangle_{BS}$ are the expectation values of the S^2 operator for the corresponding wavefunctions. Using the thermal corrections computed for the broken-symmetry solution, the free dissociation energy of **1a** amounts to 107.2 kJ/mol for dissociation into Cp*Ga and singlet ^{Dip}TerP. Assuming that the activation barrier for this process is small, the dissociative pathway lies in a similar energy window as the S_N2-type substitution with PMe_3, so it could be a (minor) contributing factor to thermal reverse reaction.

It is worthy to note that the dissociation energy compares well with the experimental activation barrier for thermal decomposition of **1a** ($t_{1/2}$ = 2866±15 min, *i.e.*, $\Delta G^{\ddagger} \approx$ 104±5 kJ/mol; cf. section 3.1), that is, dissociation of **1a** could play a role in its thermal decomposition.

Figure S41. Left: Computed thermal reaction pathway (B3LYP-D3/def2-TZVP, $c°$ = 1 mol/L). Right: Dissociation leading to singlet (S) or triplet (T) phosphinidene. Value in brackets computed by spin decontamination of the BS solution.

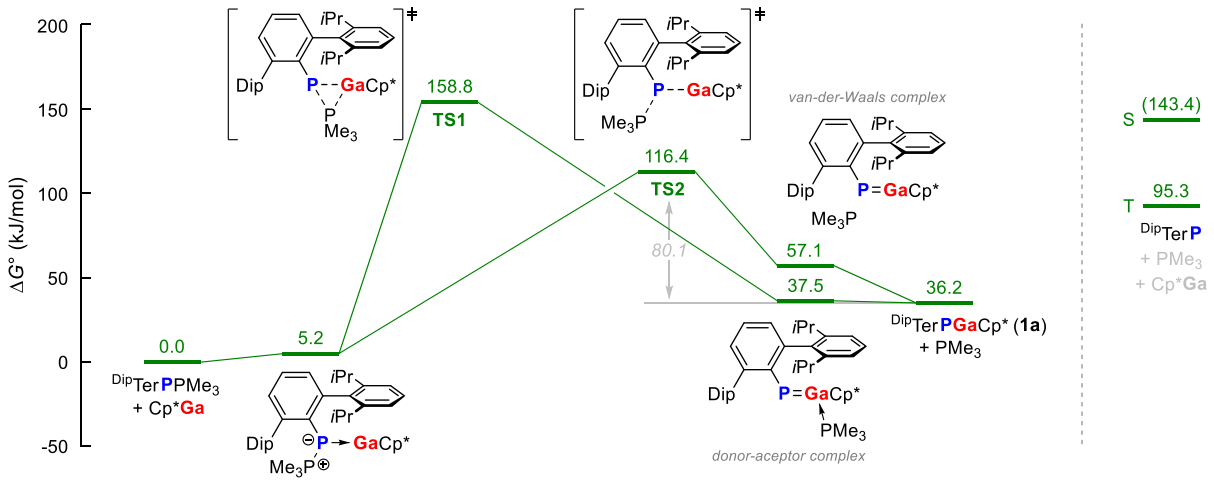

With respect to the kinetic models **i** and **ii** discussed in section 4.2, it should be pointed out that model **ii** predicts a free reaction energy for the first step (*i.e.*, the dissociation

of **1a**) of 17±66 kJ/mol, which despite its large error margin does not correspond well to the calculated data (ΔG_{diss} = 107.2 kJ/mol). Seeing that the experimental and calculated data for model **i** are in overall good agreement, we think that the S_N2-type mechanism according to model **i** is more likely than the dissociative pathway according to model **ii**.

Finally, the photochemical decomposition of ^{Dip}TerPPMe$_3$ as well as the thermal decomposition of **1a** to compound **2a** are highly exergonic at −70.4 and −106.6 kJ/mol, respectively, in agreement with experimental observation.

6 References

1 (a) Loos, D.; Schnöckel, H. (Cyclopentadienyl)-Gallium(I)-Verbindungen. *J. Organomet. Chem.* **1993**, *463* (1), 37-40; (b) Jutzi, P.; Schebaum, L. O. A novel synthetic route to pentaalkylcyclopentadienylgallium(I) compounds. *J. Organomet. Chem.* **2002**, *654* (1), 176-179.

2 Gupta, P.; Siewert, J.-E.; Wellnitz, T.; Fischer, M.; Baumann, W.; Beweries, T.; Hering-Junghans, C. Reactivity of phospha–Wittig reagents towards NHCs and NHOs. *Dalton Trans.* **2021**, *50*, 1838–1844.

3 Shah, S.; Simpson M. C.; Smith, R. C.; Protasiewicz, J. D., Three Different Fates for Phosphinidenes Generated by Photocleavage of Phospha-Wittig Reagents ArP=PMe_3. *J. Am. Chem. Soc.* **2001**, *123*, 6925–6926.

4 G. M. Sheldrick, *Acta Cryst. A* **2015**, *71*, 3–8.

5 G. M. Sheldrick, *Acta Cryst. C* **2015**, *71*, 3–8.

6 G. M. Sheldrick, *SADABS Version 2*, University of Göttingen, Germany, **2004**.

7 Merill, W. A.; Rivard, E.; DeRopp, J. S.; Wang, X.; Ellis, B. D.; Fettinger, J. C.; Wrackmeyer, B.; Power, P. P., Synthesis and Characterization of the M(II) (M = Ge, Sn, or Pb) Phosphinidene Dimers $\{M(\mu\text{-}PAr')\}_2$ (Ar′ = C_6H_3-2,6-(C_6H_3-2,6-$Pri_2)_2$). *Inorg. Chem.* **2010**, *49*, 8481–8486

8 Beer, H.; Bresien, J.; Michalik, D.; Schulz, A.; Villinger, A. Reversible Switching between Housane and Cyclopentanediyl Isomers: An Isonitrile-Catalysed Thermal Reverse Reaction. *Dalton Trans.* **2020**, *49*, 13986–13992.

9 (a) Neese, F. The ORCA Program System. *Wiley Interdiscip. Rev. Comput. Mol. Sci.* **2012**, *2* (1), 73–78; (b) Neese, F. Software Update: The ORCA Program System, Version 4.0. *Wiley Interdiscip. Rev. Comput. Mol. Sci.* **2018**, *8* (1), e1327; (c) Neese, F. Software Update: The ORCA Program System—Version 5.0. *Wiley Interdiscip. Rev. Comput. Mol. Sci.* **2022**, No. February, e1606. (d) Neese, F.; Wennmohs, F.; Becker, U.; Riplinger, C. The ORCA Quantum Chemistry Program Package. *J. Chem. Phys.* **2020**, *152* (22), 224108.

10 Frisch, M. J.; Trucks, G. W.; Schlegel, H. B.; Scuseria, G. E.; Robb, M. A.; Cheeseman, J. R.; Scalmani, G.; Barone, V.; Mennucci, B.; Peterson, G. A.; Nakatsuji, H.; Caricato, M.; Li, X.; Hratchian, H. P.; Izmaylov, A. F.; Bloino, J.; Zheng, G.; Sonnenberg, J. L.; Hada, M.; Ehara, M.; Toyota, K.; Fukuda, R.; Hasegawa, J.; Ishida, M.; Nakajima, T.; Honda, Y.; Kitao, O.; Nakai, H.; Vreven, T.; Montgomery Jr., J. A.; Peralta, J. E.; Ogliaro, F.; Bearpark, M.; Heyd, J. J.; Brothers, E.; Kudin, K. N.; Staroverov, V. N.; Keith, T.; Kobayashi, R.; Normand, J.; Raghavachari, K.; Rendell, A.; Burant, J. C.; Iyengar, S. S.; Tomasi, J.; Cossi, M.; Rega, N.; Millam, J. M.; Klene, M.; Know, J. E.; Cross, J. B.; Bakken, V.; Adamo, C.; Jaramillo, J.; Gomperts, R.; Stratmann, R. E.; Yazyev, O.; Austin, A. J.; Cammi, R.; Pomelli, C.; Ochterski, J. W.; Martin, R. L.; Morokuma, K.; Zakrezewski, V. G.; Voth, G. A.; Salvador, P.; Dannenberg, J. J.; Dapprich, S.; Daniels, A. D.; Farkas, O.; Foresman, J. B.; Ortiz, J. V.; Cioslowski, J.; Fox, D. J. Gaussian 09, Revision E.01. Gaussian Inc.: Wallingford CT **2013**.

11 Bannwarth, C.; Caldeweyher, E.; Ehlert, S.; Hansen, A.; Pracht, P.; Seibert, J.; Spicher, S.; Grimme, S. Extended tight-binding quantum chemistry methods. *WIREs Comput. Mol. Sci.* **2020**, *11*, e01493.

12 (a) Weinhold, F.; Carpenter, J. E. The Natural Bond Orbital Lewis Structure Concept for Molecules, Radicals, and Radical Ions. In *The Structure of Small Molecules and Ions*; Naaman, R., Vager, Z., Eds.; Springer: Boston, MA, 1988; pp

227–236. (b) Weinhold, F.; Landis, C. R. *Discovering Chemistry with Natural Bond Orbitals*; John Wiley & Sons, Inc.: Hoboken, NJ, USA, 2012. (c) Glendening, E. D.; Badenhoop, J. K.; Reed, A. E.; Carpenter, J. E.; Bohmann, J. A.; Morales, C. M.; Landis, C. R.; Weinhold, F. NBO 6.0. Theoretical Chemistry Institute, University of Wisconsin: Madison, WI **2013**. (10) Weinhold, F.; Landis, C. R.; Glendening, E. D. What Is NBO Analysis and How Is It Useful? *Int. Rev. Phys. Chem.* **2016**, *35* (3), 399–440.

13 Lu, T.; Chen, F. Multiwfn: A Multifunctional Wavefunction Analyzer. *J. Comput. Chem.* **2012**, *33* (5), 580–592.

14 (a) Vosko, S. H.; Wilk, L.; Nusair, M. Accurate Spin-Dependent Electron Liquid Correlation Energies for Local Spin Density Calculations: A Critical Analysis. *Can. J. Phys.* **1980**, *58* (8), 1200–1211; (b) Lee, C.; Yang, W.; Parr, R. G. Development of the Colle-Salvetti Correlation-Energy Formula into a Functional of the Electron Density. *Phys. Rev. B* **1988**, *37* (2), 785–789; (c) Becke, A. D. Density-Functional Exchange-Energy Approximation with Correct Asymptotic Behavior. *Phys. Rev. A* **1988**, *38* (6), 3098–3100; (d) Miehlich, B.; Savin, A.; Stoll, H.; Preuss, H. Results Obtained with the Correlation Energy Density Functionals of Becke and Lee, Yang and Parr. *Chem. Phys. Lett.* **1989**, *157* (3), 200–206; (e) Becke, A. D. Density-functional Thermochemistry. III. The Role of Exact Exchange. *J. Chem. Phys.* **1993**, *98* (7), 5648–5652; (f) Stephens, P. J.; Devlin, F. J.; Chabalowski, C. F.; Frisch, M. J. Ab Initio Calculation of Vibrational Absorption and Circular Dichroism Spectra Using Density Functional Force Fields. *J. Phys. Chem.* **1994**, *98* (45), 11623–11627.

15 (a) Grimme, S.; Antony, J.; Ehrlich, S.; Krieg, H. A Consistent and Accurate Ab Initio Parametrization of Density Functional Dispersion Correction (DFT-D) for the 94 Elements H-Pu. *J. Chem. Phys.* **2010**, *132* (15), 154104; (b) Grimme, S.; Ehrlich, S.;

Goerigk, L. Effect of the Damping Function in Dispersion Corrected Density Functional Theory. *J. Comput. Chem.* **2011**, *32* (7), 1456–1465.

16 Weigend, F.; Ahlrichs, R. Balanced Basis Sets of Split Valence, Triple Zeta Valence and Quadruple Zeta Valence Quality for H to Rn: Design and Assessment of Accuracy. *Phys. Chem. Chem. Phys.* **2005**, *7* (18), 3297–3305.

17 Weigend, F. Accurate Coulomb-Fitting Basis Sets for H to Rn. *Phys. Chem. Chem. Phys.* **2006**, *8* (9), 1057.

18 Neese, F.; Wennmohs, F.; Hansen, A.; Becker, U. Efficient, Approximate and Parallel Hartree–Fock and Hybrid DFT Calculations. A 'Chain-of-Spheres' Algorithm for the Hartree–Fock Exchange. *Chem. Phys.* **2009**, *356* (1–3), 98–109.

19 Alecu, I. M.; Zheng, J.; Zhao, Y.; Truhlar, D. G. Computational Thermochemistry: Scale Factor Databases and Scale Factors for Vibrational Frequencies Obtained from Electronic Model Chemistries. *J. Chem. Theory Comput.* **2010**, *6* (9), 2872–2887.

20 (a) London, F. Théorie Quantique Des Courants Interatomiques Dans Les Combinaisons Aromatiques. *J. Phys. Radium* **1937**, *8* (10), 397–409; (b) McWeeny, R. Perturbation Theory for the Fock-Dirac Density Matrix. *Phys. Rev.* **1962**, *126* (3), 1028–1034; (c) Ditchfield, R. Self-Consistent Perturbation Theory of Diamagnetism. *Mol. Phys.* **1974**, *27* (4), 789–807; (d) Wolinski, K.; Hinton, J. F.; Pulay, P. Efficient Implementation of the Gauge-Independent Atomic Orbital Method for NMR Chemical Shift Calculations. *J. Am. Chem. Soc.* **1990**, *112* (23), 8251–8260; (e) Cheeseman, J. R.; Trucks, G. W.; Keith, T. A.; Frisch, M. J. A Comparison of Models for Calculating Nuclear Magnetic Resonance Shielding Tensors. *J. Chem. Phys.* **1996**, *104* (14), 5497–5509.

21 (a) Perdew, J. P.; Burke, K.; Ernzerhof, M. Generalized Gradient Approximation Made Simple. *Phys. Rev. Lett.* **1996**, *77* (18), 3865–3868; (b) Perdew, J. P.; Burke, K.; Ernzerhof, M. Generalized Gradient Approximation Made Simple [Phys. Rev. Lett. 77, 3865 (1996)]. *Phys. Rev. Lett.* **1997**, *78* (7), 1396–1396; (c) Adamo, C.; Barone, V. Toward Reliable Density Functional Methods without Adjustable Parameters: The PBE0 Model. *J. Chem. Phys.* **1999**, *110* (13), 6158–6170.

22 Jameson, C. J.; De Dios, A.; Keith Jameson, A. Absolute Shielding Scale for ^{31}P from Gas-Phase NMR Studies. *Chem. Phys. Lett.* **1990**, *167* (6), 575–582.

23 van Wüllen, C. A Comparison of Density Functional Methods for the Calculation of Phosphorus-31 NMR Chemical Shifts. *Phys. Chem. Chem. Phys.* **2000**, *2* (10), 2137–2144.

24 (a) Bauernschmitt, R.; Ahlrichs, R. Treatment of Electronic Excitations within the Adiabatic Approximation of Time Dependent Density Functional Theory. *Chem. Phys. Lett.* **1996**, *256* (4–5), 454–464; (b) Stratmann, R. E.; Scuseria, G. E.; Frisch, M. J. An Efficient Implementation of Time-Dependent Density-Functional Theory for the Calculation of Excitation Energies of Large Molecules. *J. Chem. Phys.* **1998**, *109* (19), 8218–8224; (c) Casida, M. E.; Jamorski, C.; Casida, K. C.; Salahub, D. R. Molecular Excitation Energies to High-Lying Bound States from Time-Dependent Density-Functional Response Theory: Characterization and Correction of the Time-Dependent Local Density Approximation Ionization Threshold. *J. Chem. Phys.* **1998**, *108* (11), 4439–4449.

25 (a) Dunning Jr., T. H. Gaussian Basis Sets for Use in Correlated Molecular Calculations. I. The Atoms Boron through Neon and Hydrogen. *J. Chem. Phys.* **1989**, *90* (2), 1007–1023; (b) Kendall, R. A.; Dunning Jr., T. H.; Harrison, R. J. Electron Affinities of the First-Row Atoms Revisited. Systematic Basis Sets and Wave Functions. *J. Chem. Phys.* **1992**, *96* (9), 6796–6806; (c) Woon, D. E.; Dunning

Jr., T. H. Gaussian Basis Sets for Use in Correlated Molecular Calculations. X. The Atoms Aluminum through Argon Revisited. *J. Chem. Phys.* **1993**, *98*, 1358–1371; (d) Peterson, K. A.; Woon, D. E.; Dunning Jr., T. H. Benchmark Calculations with Correlated Molecular Wave Functions. IV. The Classical Barrier Height of the H+H2→H2+H Reaction. *J. Chem. Phys.* **1994**, *100* (10), 7410–7415; (e) Hashimoto, T.; Hirao, K.; Tatewaki, H. Comment on Dunning's Correlation-Consistent Basis Sets. *Chem. Phys. Lett.* **1995**, *243* (1–2), 190–192; (f) Wilson, A. K.; van Mourik, T.; Dunning Jr., T. H. Gaussian Basis Sets for Use in Correlated Molecular Calculations. VI. Sextuple Zeta Correlation Consistent Basis Sets for Boron through Neon. *J. Mol. Struct. THEOCHEM* **1996**, *388*, 339–349.

26 Becke, A. D.; Edgecombe, K. E. A Simple Measure of Electron Localization in Atomic and Molecular Systems. *J. Chem. Phys.* **1990**, *92* (9), 5397.

27 (a) Bader, R. F. W. Atoms in Molecules. *Acc. Chem. Res.* **1985**, *18* (1), 9–15; (b) Bader, R. F. W. *Atoms in Molecules: A Quantum Theory*; Oxford University Press, 1994.

28 Mills, G.; Jónsson, H.; Schenter, G. K. Reversible Work Transition State Theory: Application to Dissociative Adsorption of Hydrogen. *Surf. Sci.* **1995**, *324* (2–3), 305–337; (b) Jónsson, H.; Mills, G.; Jacobsen, K. W. Nudged Elastic Band Method for Finding Minimum Energy Paths of Transitions. In *Classical and Quantum Dynamics in Condensed Phase Simulations*; World Scientific, 1998; pp 385–404; (c) Henkelman, G.; Jónsson, H. Improved Tangent Estimate in the Nudged Elastic Band Method for Finding Minimum Energy Paths and Saddle Points. *J. Chem. Phys.* **2000**, *113* (22), 9978–9985; (d) Henkelman, G.; Uberuaga, B. P.; Jónsson, H. A Climbing Image Nudged Elastic Band Method for Finding Saddle Points and Minimum Energy Paths. *J. Chem. Phys.* **2000**, *113* (22), 9901–9904; (e) Maras, E.; Trushin, O.; Stukowski, A.; Ala-Nissila, T.; Jónsson, H. Global Transition Path

Search for Dislocation Formation in Ge on Si(001). *Comput. Phys. Commun.* **2016**, *205*, 13–21; (f) Ásgeirsson, V.; Birgisson, B. O.; Bjornsson, R.; Becker, U.; Neese, F.; Riplinger, C.; Jónsson, H. Nudged Elastic Band Method for Molecular Reactions Using Energy-Weighted Springs Combined with Eigenvector Following. *J. Chem. Theory Comput.* **2021**, *17* (8), 4929–4945.

29 (a) Baker, J. An Algorithm for the Location of Transition States. *J. Comput. Chem.* **1986**, *7* (4), 385–395; (b) Schlegel, H. B. Optimization of Equilibrium Geometries and Transition Structures. In *Advances in Chemical Physics: Ab Initio Methods in Quantum Chemistry Part I, Volume 67*; Lawley, K. P., Ed.; John Wiley & Sons, 1987; pp 249–286; (c) Schlegel, H. B. GEOMETRY OPTIMIZATION ON POTENTIAL ENERGY SURFACES. In *Modern Electronic Structure Theory*; Yarkony, D. R., Ed.; World Scientific, 1995; pp 459–500; (d) Eckert, F.; Pulay, P.; Werner, H.-J. Ab Initio Geometry Optimization for Large Molecules. *J. Comput. Chem.* **1997**, *18* (12), 1473–1483.

30 Grimme, S. Exploration of Chemical Compound, Conformer, and Reaction Space with Meta-Dynamics Simulations Based on Tight-Binding Quantum Chemical Calculations. *J. Chem. Theory Comput.* **2019**, *155*, 2847-2862.

31 Bannwarth, C.; Ehlert, S.; Grimme, S. GFN2-xTB—An Accurate and Broadly Parametrized Self-Consistent Tight-Binding Quantum Chemical Method with Multipole Electrostatics and Density-Dependent Dispersion Contributions. *J. Chem. Theory Comput.* **2019**, *15*, 1652-1671.

32 Silva Lopez, C.; R. de Lera, A. Bond Ellipticity as a Measure of Electron Delocalization in Structure and Reactivity. *Curr. Org. Chem.* **2011**, *15* (20), 3576–3593.

33 Stalke, D. Charge Density and Chemical Bonding. In *The Chemical Bond I. Structure and Bonding, Volume 169*; Mingos, D. M. P., Ed.; Springer, Cham, 2016; pp 57–88.

34 a) Herebian, D.; Wieghardt, K. E.; Neese, F. Analysis and Interpretation of Metal-Radical Coupling in a Series of Square Planar Nickel Complexes: Correlated Ab Initio and Density Functional Investigation of [Ni(L^{ISQ})$_2$] (L^{ISQ}=3,5-di-*tert*-butyl-*o*-diiminobenzosemiquinonate(1-)). *J. Am. Chem. Soc.* **2003**, *125*, 10997–11005; b) Yamagushi, K. The electronic structures of biradicals in the unrestricted Hartree-Fock approximation. *Chem. Phys. Lett.* **1975**, *33*, 330–335.

35 Malrieu, J.-P.; Trinquier, G. A Recipe for Geometry Optimization of Diradicalar Singlet States from Broken-Symmetry Calculations. *Phys. Chem. A* **2012**, *116*, 8226–8237.